LIQUID BRIDGE TO STABLE FIBRE: POLYMER ENTANGLEMENT DRIVES FIBRE FORMATION FROM HIGHLY CONCENTRATED DEXTRAN SOLUTIONS

by

Gurkaran Chowdhry

Submitted in partial fulfillment of the requirements
for the degree of Master of Science

at

Dalhousie University
Halifax, Nova Scotia
October 2020

This thesis is dedicated to my parents, Chander and Leeza Chowdhry. Thank you for handbags full of home-cooked meals, oil changes as currency for affection, and the unconditional love that makes anywhere feel like home. Thank you for always encouraging my curiosity and never telling me to stop asking questions. None of this happens without you.

Table of Contents

List of Tables

List of Figures

Abstract

Liquid bridges have been studied for over 200 years, due to their countless natural and industrial occurrences. Majority of these studies focus on Newtonian fluids between coaxial discs, where the dimensions of the liquid bridge are on the millimeter scale. Presented in this thesis is the characterization of liquid bridges that stabilize into polymeric fibres that are 10 cm long, while being less than 20 μm in diameter. To control the fibre formation process, a horizontal single-fibre contact drawing system was created, consisting of a motorized stage, a micro-needle, and a liquid filled reservoir. Analyzing liquid bridge rupture statistics as a function of elongation speed and solution properties revealed that a single timescale governed the fibre formation process. Using the reptation model for the viscoelasticity of the entangled polymer solution showed that this timescale corresponded to the relaxation time of entanglements. Characterization of the final fibres revealed that fibre diameter was proportional to the initial solution viscosity due to a secondary flow that occurs during the fibre formation process. Verification of these results with the addition of type I collagen demonstrates the significance of these findings in potentially using this contact drawing method for biomaterial fabrication.

List of Abbreviations Used

CaBER Capillary Breakup Extensional Rheometer.

CDF Cumulative Distribution Function.

DI Deionized.

NMR Nuclear Magnetic Resonance.

NRA Nuclear Reaction Analysis.

PDF Probability Density function.

Acknowledgements

They say it takes a village, and that was definitely true inside and outside of this degree over the last two years. The community I relied on stretched far beyond my department, but so much of that community came from within it.

Dr. Laurent Kreplak - Thank you for being endlessly supportive. No matter what I needed over the course of this degree, somehow you were always able to make it available. I will never forget when we met right before COVID shut labs down, and your first priority was to make sure that I was able to safely and comfortably stay in my home if things were to get worse. Your support never went unnoticed.

Dr. John Frampton - Thank you for always encouraging me to stay ambitious. Finding this interdisciplinary project, and being welcomed into your lab group were some of my favourite things about this degree. I'm excited to see the things we do.

I'd like to thank Tanya Timmins for being a rock, and making this department feel like home since Day 1. I'd also like to thank Dr. Ted Monchesky and Dr. Andrew Rutenberg for being such a big part in my graduate experience. I was grateful for your open door policies, and your support of things I pursued inside and outside of this degree. Dr. Stephen Payne, thank you for doing everything you do. You're a big part of the reason I get excited about a dark, clear sky.

John Lincoln, Charlotte Clegg, Dr. Tim Bardouille and Dr. Kevin Hewitt - It's been a privilege working alongside you all to tackle the barriers and inequities in our department. The work you all do is going to continue to have curious folks like myself turn to this department.

There are several graduate students who made the Dunn an exciting place to be: Brendan Brady, Liam Bindle, Cam Rudderham, Patrick Strongman, and the others in 207. Random chats and timmies runs were a huge part of getting through some days.

Last, but certainly not least, thank you Chris Peacock, Eric Bergmann, and Kelsey Gsell, for reminding how valuable the dinner table is.

Chapter 1

Introduction

1.1 Overview

Collagen fibres are the most abundant protein structure in the human body, and play a critical role in the structure of tissue. This pivotal role makes collagen a highly desirable biomaterial because it can support cell growth and has numerous applications including in cell culture, tissue regeneration, and wound care. However, collagen is not widely used in these applications because there is not yet a sustainable method to produce collagen fibres. Recently, the Frampton lab has started creating collagen fibres through a method known as contact drawing [1, 2]. In contact drawing, a highly concentrated aqueous solution of a long-chain polymer and collagen is created. This solution is then interposed between two surfaces that are subsequently pulled apart, creating liquid bridges which stabilize into fibres that can be metres long, while only being 2-20 μm in diameter. This method to produce fibres does not damage the collagen, is highly scalable, and does not require specialized equipment, motivating the potential of contact drawing as a manufacturing process of collagen fibres for biomedical applications. The goal of this thesis is to understand the physical mechanism that controls the contact drawing process, and the following sections cover the relevant background that motivated this study.

1.2 Liquid bridges

Liquid bridges define a volume of liquid with a minimized surface, suspended between two rigid bodies. These bridges have well defined stability conditions, defining the transition from one continuous volume rupturing into two droplets [3], and accompanying forces which lead to attraction or repulsion between the rigid bodies [4]. Through these conditions, liquid bridges are responsible for many natural and industrial processes [5, 6, 7]. For example, beetles, blowflies and many other insects use

liquid bridges as a wet adhesive to climb vertical surfaces [8]. Liquid bridges between the insects feet and the vertical surface generate attractive forces sufficient to carry the weight of these insects [9], and may also play a role in how larger animals such as geckos climb [10]. In an industrial setting, liquid bridges and their instability play a key role in the printing process [11]. By understanding the rupture characteristics of liquid bridges, and controlling the size and location of each droplet following rupture, industrial printing processes are able to achieve the high degree of precision they have today [11].

These various occurrences and the industrial relevance have motivated over 200 years of research in liquid bridges, dating back to Young's first report of a liquid suspended between two coaxial discs [12]. Since this report, the majority of these studies have focused on Newtonian liquids suspended between two small coaxial discs, and characterizing the resulting bridge shapes, stability limits, and accompanying forces [13, 14, 15]. Shown in Figure 1.1, this setup has a simple axisymmetric profile, and allows one to assume that the liquid bridge fully wets the small discs (millimeter

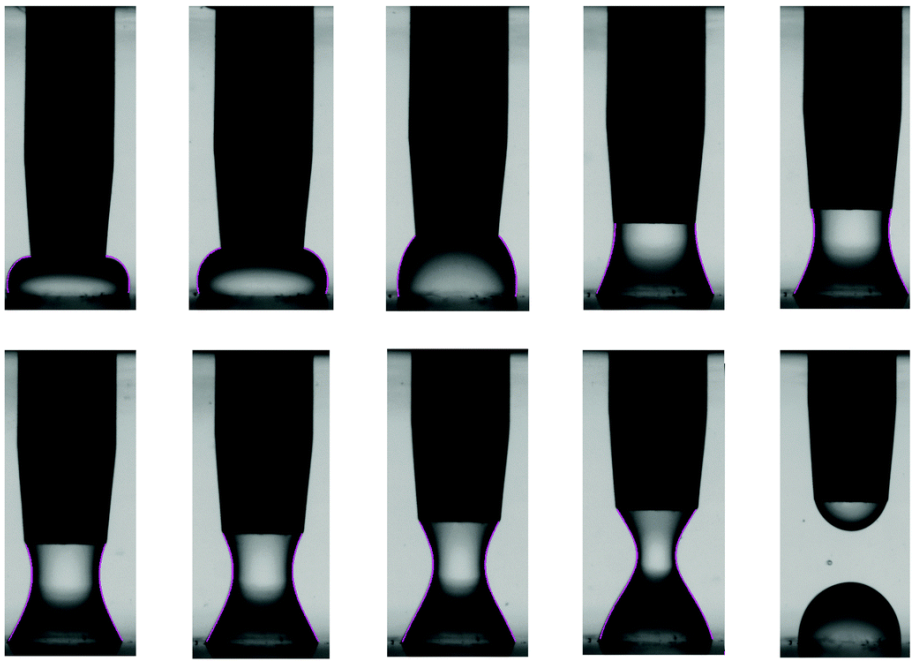

Figure 1.1: *The evolution in liquid bridge shape as the distance between two coaxial discs is increased, until rupture. The bridge is of a Newtonian fluid, silicon oil, and seen to have a curved-cylindrical or hourglass type shape. Adapted from [16] with permission from The Royal Society of Chemistry.*

scale radius). Assuming an axisymmetric profile and a fixed liquid-solid boundary simplifies experiments and simulations. The liquid bridge stability is defined by the slenderness of the bridge, the disc radii, the eccentricity of the bridge shape, the volume of liquid, the difference in density between the liquid and the surrounding gas, as well as the surface tension [17]. With these parameters, the stability shapes and limits can be solved through the Young-Laplace equation, which balances the capillary force acting on the liquid-gas interface, with the pressures exerted at this interface [18]. In general, liquid bridge rupture in this set-up occurs near the Plateau stability limit, where the ratio of the liquid bridge length (L) to the disc radii (R) at rupture is approximately 2π [19, 20]. Therefore, for Newtonian fluids suspended between two co-axial discs, the length of the bridge is of the same order as the disc radii, which is no larger than a few millimeters in most systems.

More recently, studies have shifted to characterize more complex systems, such as those with non-planar surfaces binding the liquid bridge. In using spheres, for example, as the distance between the two spheres increases, the area at the liquid-solid interface changes, invalidating the fixed boundary assumption [21]. In this geometry, by modelling liquid bridge rupture based on the thinning of the neck radius, Dai was able to solve for the shape and stability of liquid bridges between two spheres without using the Young-Laplace equation [22]. Between two spherical rigid bodies, the Newtonian liquid bridges have similar rupture characteristics to planar surfaces, with length-scales on the order of bridge radii [21, 22].

In moving away from simple Newtonian fluids to high viscosity fluids, the liquid bridge shapes and stability limits change significantly. In liquid bridge studies of aqueous glycerol solutions in the traditional coaxial disc geometry, high viscosity bridges had a much different shape than those with low viscosities [23]. Instead of a curved cylindrical shape, high viscosity liquid bridges had pronounced conical ends, connected by a long thin liquid cylinder, as shown in Figure 1.2. These bridges also had significantly longer lengths at rupture, with the liquid bridges of highest viscosity being twice as long as the liquid bridges of lowest viscosity [23]. Compared to the length-scales of traditional low viscosity liquid bridges, these high viscosity solutions led to lengths an order of magnitude greater than the bridge radii at breakup, and lifetimes on the order of 0.01 s [23].

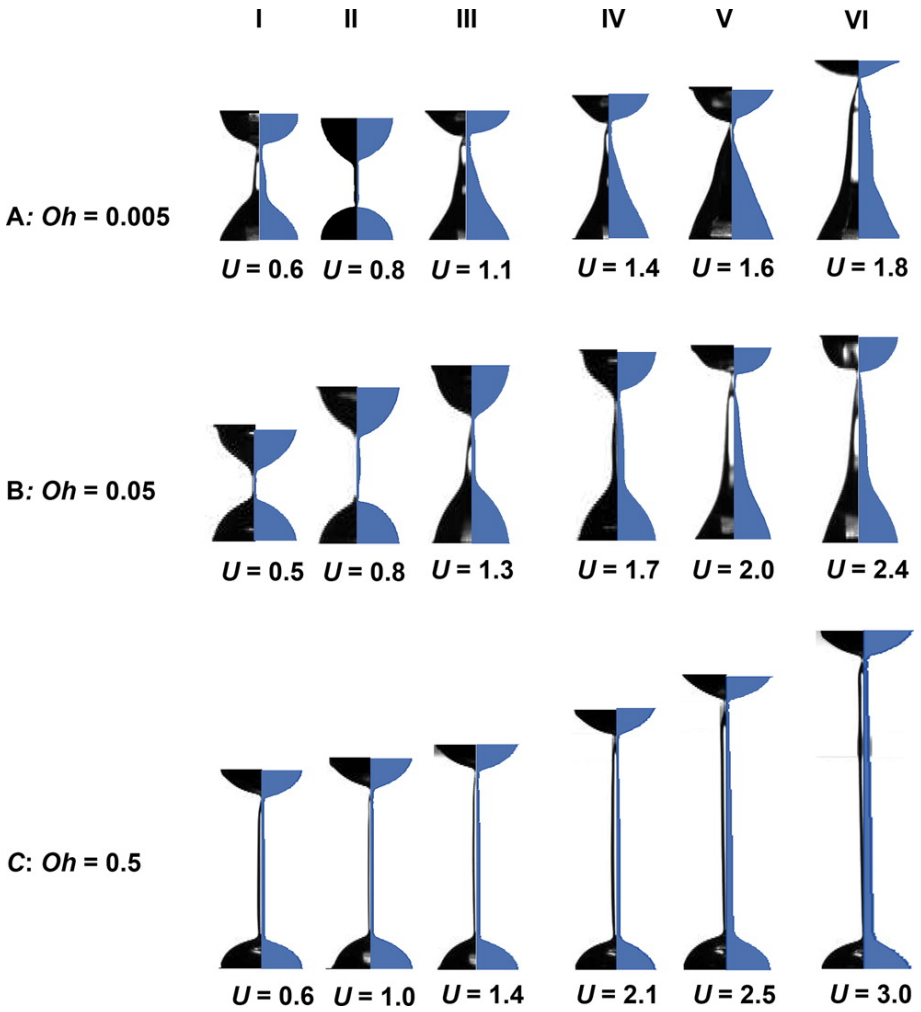

Figure 1.2: *Images right before rupture for experimentally captured (black) and predicted (blue) liquid bridges of aqueous glycerol solutions. U represents the various stretching velocities, and Oh is the Ohnesorge number defined as the ratio of the viscous forces to the inertial and surface tension forces. As viscosity increases (higher Oh), the length at rupture is seen to increase. The shape of the bridge moves further away from the hourglass shape seen in Figure 1.1, to defined conical ends connected by a long liquid thread. Figure reprinted with permission from [23]. Copyright 2015 American Chemical Society.*

Liquid bridges of methylcellulose in water, a non-Newtonian fluid, showed shapes different than the normal hour-glass and much longer lifetimes [24]. In this study, solutions were controlled to contain free methylcellulose polymers, as well as combinations of free polymers and larger methylcellulose fibrils. These polymer solutions were extended into liquid bridges using a Capillary Breakup Extensional Rheometer (CaBER), which creates 1-10 mm long liquid bridges in just a few milliseconds

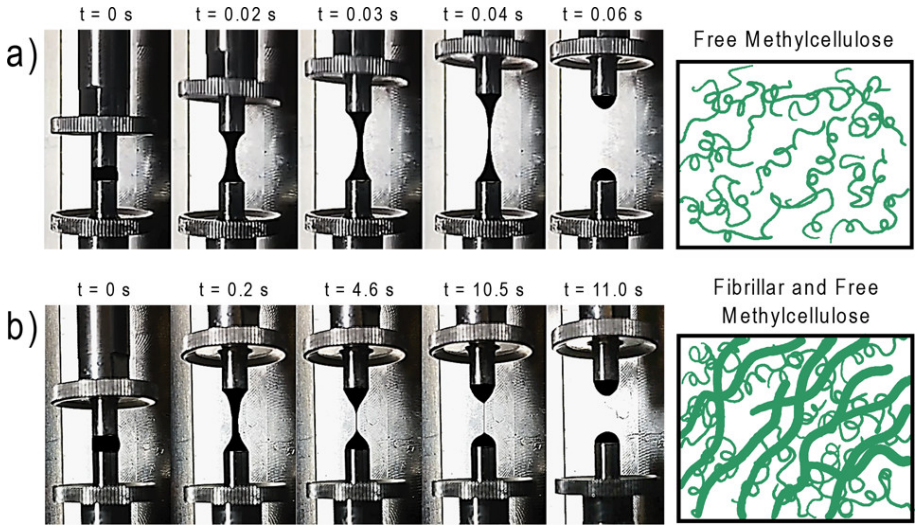

Figure 1.3: *Experimental snapshots of an aqueous solution of methylcellulose (a) without and (b) with fibrillar methylcellulose. In both cases, the shapes are not like the hourglass seen in Figure 1.1, with (b) showing a very thin thread like liquid column connecting the two conical ends. Reprinted with permission from [24]. Copyright 2018 American Chemical Society.*

[25, 26, 27]. Shown in Figure 1.3, these bridges had shapes much different than the traditional cylindrical shapes, with conical ends and an extremely thin liquid cylinder connecting these ends, and were stable for longer than 10 seconds [24]. At the highest polymer concentrations, 8-9 mm long liquid bridges were stabilized at diameters of approximately 400 μm, showing that these liquid bridges of non-Newtonian fluids enter a new length-scale regime, where the length is 20 times the radius, and the lifetimes are at least 10s of seconds. The authors suggest that entanglements of polymers or fibrils within their solution were responsible for the long term stability of these liquid bridges [24].

1.3 Polymer solutions and reptation theory

The structure and dynamics of polymer solutions are complex, and depend largely on the conformation and concentration of the polymer in the solvent. The conformations of individual chains are governed by a minimization of their free energy, which balances the monomer-solvent interaction with the entropy of the chain [28, 29, 30], and different conformations are summarized in Figure 1.4. When the polymer is in a 'poor' solvent where the monomer-solvent interaction is less energetically favourable

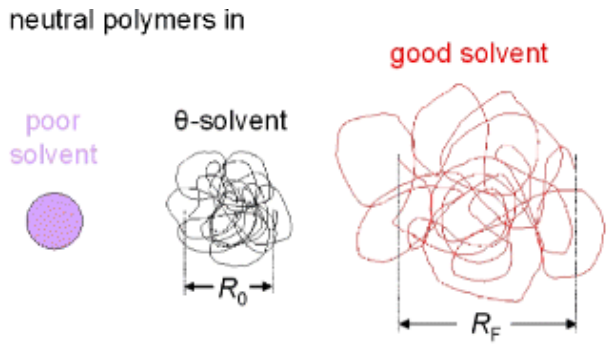

Figure 1.4: *Neutral polymer conformation is shown in poor, θ and good solvent. In poor solvent, polymer chains collapse into dense coils, in θ-solvent polymers can be modelled as a random coil, and in good solvent polymers expand to increase monomer-solvent interaction. End-to-end distances are labelled as R_0 and R_F (Flory radius) for θ and good solvents, respectively. Figure adapted from [32] with permission. Copyright 2009, Springer Nature.*

than monomer-monomer interactions, the polymer forms dense globule conformations minimizing solvent interaction and thereby minimizing free energy [29, 31]. When monomer-solvent interactions are strong then the polymer swells to maximize its interaction with the solvent. The Flory radius (R_{F}) is a result of a balance between increasing the interface with the solvent (energetically favourable) and stretching the polymer chain (entropically unfavorable) [29]. In between these two regimes exists the θ-solvent, in which monomer-monomer and monomer-solvent interactions are equally favourable. In a θ-solvent, a polymer conformation is a random walk of the polymer's subunits [32].

For polymers in θ-solvents and good solvents, the polymer conformation is defined as a random walk or a self-avoiding walk, respectively. To define the conformation as such implies that the polymer's subunits are uncorrelated, which seems counter-intuitive given polymers are a physical chain of monomer units, and two monomers cannot occupy the same volume. This condition is the excluded volume interaction, which defines the repulsion between monomer units [33]. In a polymer of N monomer units, the shape of the chain can be defined by N - 1 vectors $\vec{b}_{\mathrm{i}}$, each of which links two consecutive monomers. Therefore, the end-to-end distance of the polymer ($\vec{r}$) can be defined as [33]

$$\sum_{i=1}^{N-1} \vec{b}_{\mathrm{i}} = \vec{r}. \tag{1.1}$$

Although connected monomers will definitely be correlated in their position due to the excluded volume interactions, after some number of monomers g, where $g < N$, this correlation is lost. That is to say $\vec{b}_{\mathrm{i}}$ is independent of vector $\vec{b}_{\mathrm{i+g}}$. By defining N/g new vectors $\vec{c}_{\mathrm{i}}$, where each $\vec{c}_{\mathrm{i}} = \sum_i^g \vec{b}_{\mathrm{i}}$, the end-to-end distance of the chain can be defined as

$$\sum_{i=1}^{\frac{N}{g}-1} \vec{c}_{\mathrm{i}} = \vec{r}, \tag{1.2}$$

where the $\vec{c}_{\mathrm{i}}$ vectors are uncorrelated [33]. The distance represented by $\vec{c}_{\mathrm{i}}$ defines the persistence length, and by assuming the polymer chain is made up of spherical subunits of this persistence length, the random walk or self-avoiding walk is achievable [34]. At length-scales less than the persistence length, hydrodynamic interactions are important, and the persistence length will be characteristic of the rigidity of the polymer, as well as the monomer-solvent interactions. In this situation, $\vec{r}$ shown as R_0 and R_{F} in Figure 1.4, defines the radius of a pervaded volume occupied by the polymer.

The polymer conformation is crucial to understanding the dynamics of polymers in solution. When interacting with a polymer solution a viscoelastic response is observed, where the timescale of the interaction determines if the response is more viscous-like or more solid-like [33]. Generally, when the polymers in solution are perturbed from their equilibrium conformation they store elastic energy, allowing them to relax back to their minimized energy state [35]. However, since they are in solution, some energy from the interaction is dissipated through flow of the liquid, thereby defining the viscoelastic response [35]. The degree of viscous response to elastic response is dependent upon the timescales of relaxation, which characterize the time it takes for the perturbed polymer solution to return to equilibrium [32]. This 'degree' of viscoelasticity can be quantified by applying low amplitude oscillating shear stresses to a polymer solution, and quantifying the strain [36]. In a purely elastic material, this strain occurs in phase with the applied stress, whereas in a purely viscous solution the strain has a characteristic $\pi/2$ phase lag to the applied stress [36]. It is then expected that viscoelastic solutions have an intermediary phase behaviour, which is dependent on the frequency of oscillation as it probes the relaxation mechanics of the polymer solution over a frequency-space [36]. The underlying mechanics of the

relaxation are controlled by various properties, but a key factor is the concentration of polymer in solution [32]. For the following discussion, polymers in 'poor' solvents will no longer be discussed, as this combination is not relevant to the study.

As illustrated in Figure 1.5, in dilute solutions the concentration of polymer in solution (c) is significantly less than the concentration of polymer within it's pervaded volume. In this regime the solution dynamics are governed by the dynamics of individual chains, which depend on the solvent interactions and excluded volume interactions [32]. Thus, any viscoelastic response of a dilute solution is a result of elastic energy stored within these individual polymer chains, as they are perturbed from their equilibrium conformations [37]. As the concentration of polymer is increased, eventually the overlap concentration (c^*) is reached, where the concentration of the solution is equivalent to the concentration within the pervaded volume (Figure 1.5), and polymers are influenced by other polymer chains [38]. At a large range around $c = c^*$ the polymer solution is in the semi-dilute unentangled regime [32], where a correlation distance (ξ) can be defined as the distance between monomers of different chains, and the correlation blob is the corresponding volume. Over distances less than ξ, there are only monomers from the same chain surrounded by numerous solvent molecules, and over this lengthscale the polymer behaves as it would in dilute solution. However, at distances greater than ξ, a polymer is influenced by other polymer chains, which screen out monomer-solvent interactions. Thus, ξ describes the screening distance, and as the concentration of polymer increases, ξ decreases [40]. It then follows that in semi-dilute polymer solution there are two mechanisms governing the solution dynamics: at lengthscales longer than ξ, the monomer-solvent interactions are screened, and the polymer solution can be treated as a random walk of correlation blobs, whereas at lengthscales shorter than ξ the polymer subunits act as polymers in dilute solution [34]. In recovering from perturbations towards equilibrium, this results in two distributions of relaxation times, the longer of which corresponds to the relaxation of the correlation blobs [32].

For this study, the most relevant regime is the entangled regime, at concentrations above the entanglement concentration (c_e) [32]. Although a clear understanding is yet to be developed, c_e is greater than and proportional to c^*, and in some cases is on the order of 10 times larger [32]. At these high concentrations, polymers in θ and

'good' solvents are largely overlapped and if treated as linear chains, begin to tangle together (Figure 1.5), moving them out of the semi-dilute regime, into the entangled regime. Within the entangled regime, the longest relaxation time corresponding to the relaxation of entanglements can be defined using reptation theory [41, 42]. In this model, a polymer in a highly concentrated solution is confined to a tube, where the sides of the tube are defined by the physical barriers presented by other polymers in solution as shown in Figure 1.6. At each of these intersections, the polymer cannot translate laterally through other polymers and therefore can only move along the one-dimensional tube defined by these boundaries [41]. The radius of this tube, a_{tube}, is larger then the correlation distance ξ, and thus the polymer can be treated as a chain of correlation blobs within the tube [42]. Thus, the chain length can be defined as

$$L_{\text{t}} = \frac{N}{g}\xi \tag{1.3}$$

where L_{t} is the chain length and $\frac{N}{g}$ is the number of correlation blobs in a chain [34]. Since the chain is subject to thermal fluctuations, there is an accompanying diffusion coefficient defined as

$$D_{\text{t}} = B\frac{k_{\text{b}}T}{N}, \tag{1.4}$$

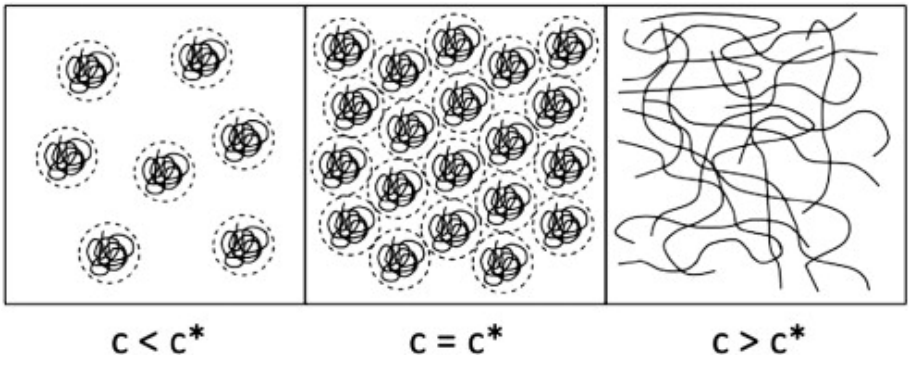

Figure 1.5: *The different concentration regimes of a polymer solution are shown. At c $< c^*$, the concentration of the solution is much less than the concentration within the pervaded volume of each polymer, defining the dilute regime. At the overlap concentration, $c = c^*$, solutions are in the semi-dilute regime where the solution concentration is equal to the concentration of polymer within the pervaded volume. In the highly concentrated entangled regime, $c > c^*$, polymers are overlapped and entangled. Reproduced from [39] with permission.*

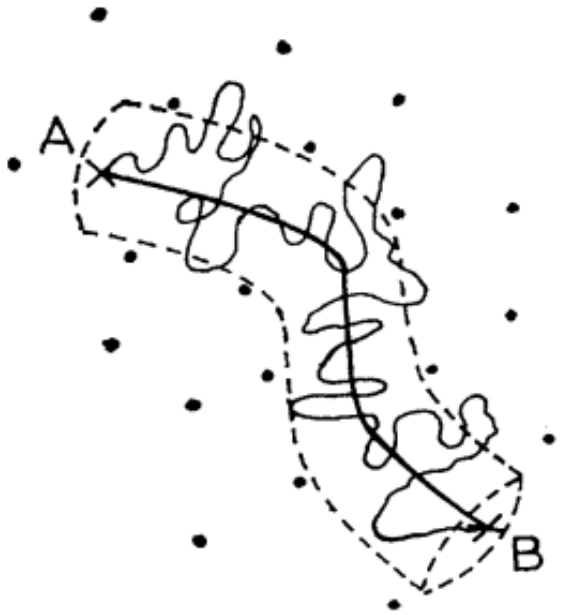

Figure 1.6: *A polymer chain is shown inside its confinement tube, where the dots represent other chains which, in this drawing, are assumed to be perpendicular to the paper. Due to entanglements the chain is confined to the tube-like region denoted by the broken line. The bold line shows the primitive path. Reproduced from [41] with permission from The Royal Society of Chemistry.*

where D_t is the diffusion coefficient, B is the monomer mobility (characterising frictional and drag forces in the solution), k_b is Boltzmann's constant and T is the temperature [34]. It is important to note that D_t is inversely proportional to N, meaning longer chains are less mobile. By characterizing the length of the confinement tube, and the diffusion coefficient, the time required by the chain to diffuse out of the tube can be defined as

$$\tau_\mathrm{rep} = \frac{{L_\mathrm{t}}^2}{D_\mathrm{t}} = \left(\frac{N}{g}\xi\right)^2 \left(\frac{1}{B}\right) \left(\frac{N}{k_\mathrm{b}T}\right), \tag{1.5}$$

where τ_rep is the characteristic time it takes a polymer to completely abandon its tube and the corresponding entanglements, and enter a new tube [33]. τ_rep can be on the scale of seconds in an entangled polymer solution, and is the longest relaxation time of the polymer solution [32]. Therefore, the dynamics of polymers and their entanglements govern the dynamics of entangled polymer solutions. If interacting with a polymer solution at timescales much greater than τ_rep, entanglements are freely abandoned and a viscous flow is observed [36]. At timescales significantly shorter than

τ_{rep}, entanglements are locked in and the mechanics are governed by the relaxation of monomers within the polymer chains, as would be expected from a solid. However, when the interaction times are on the order of τ_{rep}, viscoelastic responses are observed where some energy is elastically stored in the distorted entanglement network, whereas the remaining energy is dissipated through viscous flow of the polymer solution [36].

Experimentally, there is no direct way to measure τ_{rep}, but by using experimental techniques to probe the conformation of polymer chains and the diffusion rates, τ_{rep} can be calculated. The conformation of the polymer can be determined by a variety of techniques including small angle neutron scattering, which allows a direct measurement of the end-to-end distance of a polymer [43]. Since the degree of polymerization is usually known for a selected polymer, by treating the end-to-end distance as a random walk, the correlation length can be determined as the step size that allows for this random walk. The diffusion coefficient can be measured using specialized techniques such as Nuclear Reaction Analysis (NRA). NRA is a nuclear spectroscopy technique, in which a sample is irradiated by nuclei of defined energies, leading to a nuclear reaction with a sharply defined resonance energy [44]. Through this reaction, a nucleus is usually in an excited state, leading to an immediate decay, which emits radiation that can be detected and characterized. In one experiment to characterize the diffusion of polymers in entangled solutions, two thin polymeric films were made with high M_w protonated and deuterated polystyrene, respectively [45]. When brought into contact at higher temperatures, a sharp interface existed at first, but over time the polymers from each thin film could diffuse into the other. Based on reptation theory, only those polymers with free ends near the interface would be able to diffuse, and as this occurred at the interface, the depth of interpenetration was characterized using NRA, as a function of time, allowing a calculation of the diffusion coefficient [45]. Coupled with the neutron scattering measurement for the correlation length, this allows a calculation of τ_{rep}. Although other techniques can be used to quantify this diffusion, such as Nuclear Magnetic Resonance (NMR) spectroscopy [46], dielectric spectroscopy [47], and fluorescence microscopy [48], they are often just as complicated.

1.4 Collagen fibre manufacturing and contact drawing

At the end of section 1.2 was the presentation of liquid bridges that were stable for 10s of seconds and others that were fully stable. In the report, the authors argued that this long term stability was due to the relaxation time of entanglements within their methylcellulose solutions [24]. In the case where entanglements form during the liquid bridge process, these entanglements are accompanied by elastic properties which would stabilize the liquid bridges [49]. Stablized liquid bridges of a biopolymer such as methylcellulose show the potential application of using liquid bridges to create fibres containing biological and biocompatiable materials, which has been an extensive interest for both academic and industrial research.

One example of this is in creating properly assembled collagen fibres. Collagen is the most abundant protein in the human body, and plays a critical role in the structure and architecture of various tissues [50]. With over 29 sub-types of collagen, the most abundant collagen is type I, which has a fibrillar architecture and is essential for maintaining structure and function of tissues [51, 52]. As such, type I collagen has many biomaterial applications, including in cell culture, tissue engineering, and regenerative medicine. Currently, isolated collagen molecules in solution are commercially available, but developing assembled collagen structures for cell and tissue growth has been a long-standing challenge.

At the moment, one of the most popular techniques for fabricating synthetic collagen fibres is electrospinning [53]. The traditional electrospinning setup is shown in Figure 1.7. Polymer solutions, often in volatile solvents, are extruded through a narrow pipette using a pump [54]. Once a droplet has formed, the tip of the pipette is subject to tens of kilovolts. Due to this, the charge repulsion within the droplet overcomes the surface tension holding the droplet, and a jet of solution is expelled towards the grounded substrate [55]. As the liquid is projected towards the substrate, the volatile solvent rapidly evaporates, and a polymeric fibre is formed. During this 'jetting' process, the fibre is subjected to extremely high accelerations, which stretch the fibre and lead to the sub-micron fibre diameters obtained by this technique [56, 57]. To form fibres however, the polymer solutions must be in the entangled regime, as entanglement is necessary to stabilize the polymer jet [58]. The relaxation times associated with polymer entanglements must be long enough that

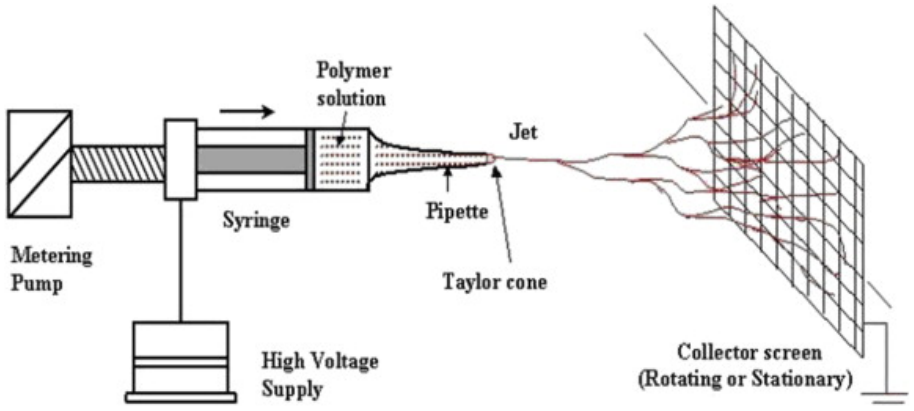

Figure 1.7: *A schematic of the electrospinning setup is shown here. A polymer solution is extruded to a narrow pin, and subjected to an extremely high voltage. The charge repulsion expels the solution towards the grounded substrate, during which time solvent evaporates and a fibre is formed. Image reprinted from [54] with permission.*

adequate evaporation of solvent can occur, forming a stable fibre. In cases where the concentration is lower, electrospun fibres are seen to have beaded structures, and at concentrations significantly lower than the entanglement concentration, this process only produces droplets and is known as electrospraying [58].

With the addition of collagen, electrospinning can produce sub-micron fibrillar structures which are similar to native collagen, and these structures can be collected with some control over the alignment and porosity [59]. However, electrospinning requires highly specialized equipment in order to obtain the tens of kilovolts needed for the process [54]. Furthermore, electrospun fibres are often subject to volatile solvents and extremely high shear rates, which can denature the collagen, making the fibres inadequate for the desired final applications [60, 61, 62]. To overcome the volatile solvents and high shear rates of electrospinning, another popular technique to produce collagen fibres is wet-spinning [63, 64]. In wet-spinning, a collagen solution is slowly extruded through a 100-400 μm hole into a coagulation bath which forms the liquid stream into a gel-like collagen fibre [64]. These gel-like fibres are subsequently dried and stretched to form the final fibre. Although this method preserves the structure of collagen molecules, it is extremely slow, producing only a single relatively large (>20 μm diameter) fibre [63, 64].

As an alternative to these methods, the Frampton lab has shown that a 50 %wt solution of dextran in water which is interposed between two flat surfaces that are

then pulled apart, can from an array of stable polymer fibres 10s of micrometers in diameter and meters in length [1]. This process has since been called contact drawing. By integrating collagen and creating 3D structures, contact drawn collagen-containing fibres were able to support aligned cell growth, showing their potential as a biomaterial in cell culture and regenerative medicine [2]. However, the mechanism for fibre formation and the structure of final fibres has not previously been fully characterized.

1.5 Motivation for the current work

The goal of this thesis is to uncover the underlying mechanism of fibre formation in the contact drawing process. The contact drawing process has dynamics related to all of the preceding subsections. Starting with a polymer solution interposed between two flat surfaces, that are subsequently pulled apart, contact drawing creates liquid bridges of polymer solutions. However, unlike any liquid bridge studies, contact drawing exists in a regime where the length of the bridges is at least 3-4 orders of magnitude greater than the radius. Since these polymer solutions are extremely concentrated, the polymer dynamics are likely in the entangled regime, and thus exhibit viscoelastic effects. The result of forming stable fibres resembles the electrospinning process, where a balance between relaxation time and solvent evaporation is critical to fibre formation. With these existing processes, fibre formation in contact drawing was analyzed. A horizontal contact drawing system was developed, which allowed single fibre formation to occur. This experimental system used a motorized linear stage, allowing precise control over the length and speed at which fibres were formed. By controlling the solution properties (dextran molecular weight and concentration) and the interaction time with the solution, the success of fibre formation was characterized with a focus on polymer entanglements. Additionally, to understand the final fibre structures, the fibre diameters were characterized with solution properties and fibre formation conditions.

Chapter 2

Materials and Methods

2.1 Overview

This section describes the materials used throughout the experiments, the custom made experimental apparatus, and the experimental and analytical steps for the various parts of this study. Appendix A contains the designs for all 3D printed parts, Appendix B outlines preliminary data that informed this final experimental design, and Appendix C contains solution characterization data.

2.2 Experimental setup

In order to understand the fibre formation process, an experimental apparatus capable of drawing single fibres was created, and is shown in Figure 2.1. To draw fibres, a steel micro-needle with a tip diameter of 0.1 mm and a shank diameter of 0.5 mm was purchased from Ted Pella (product no. 13601C). The micro-needle was screwed into a Ted Pella Micro-Tool Handle (product no. 13600), which has a diameter of approximately 7 mm and a length of 120 mm. For controlling the movement of the micro-needle, the handle was mounted onto a 100 mm linear translation stage (Thorlabs DDSM100/M), using 3D printed mounts. The mounting system consisted of two blocks with cylindrical cavities to hold the handle, which was fixed with set screws. All 3D printed parts were made of B9R 2 BlACK photopolymer resin using a B9 Creator 3D printer, and all CAD drawings are shown in Appendix A.

The stage was operated with the Kinesis software from Thorlabs, in which a simple program was written to control the speed and the distance of travel. To calibrate the actual speed, the stage was programmed to move the entire distance of the stage (100 mm) at a set speed, stop for 2 s, and travel the entire distance again at the same speed. This 2 step movement was recorded using an Edgertronic high speed camera fitted with a Nikon Nikkor 50 mm lens, in increments of 60 mm/s, from 2-600 mm/s (as

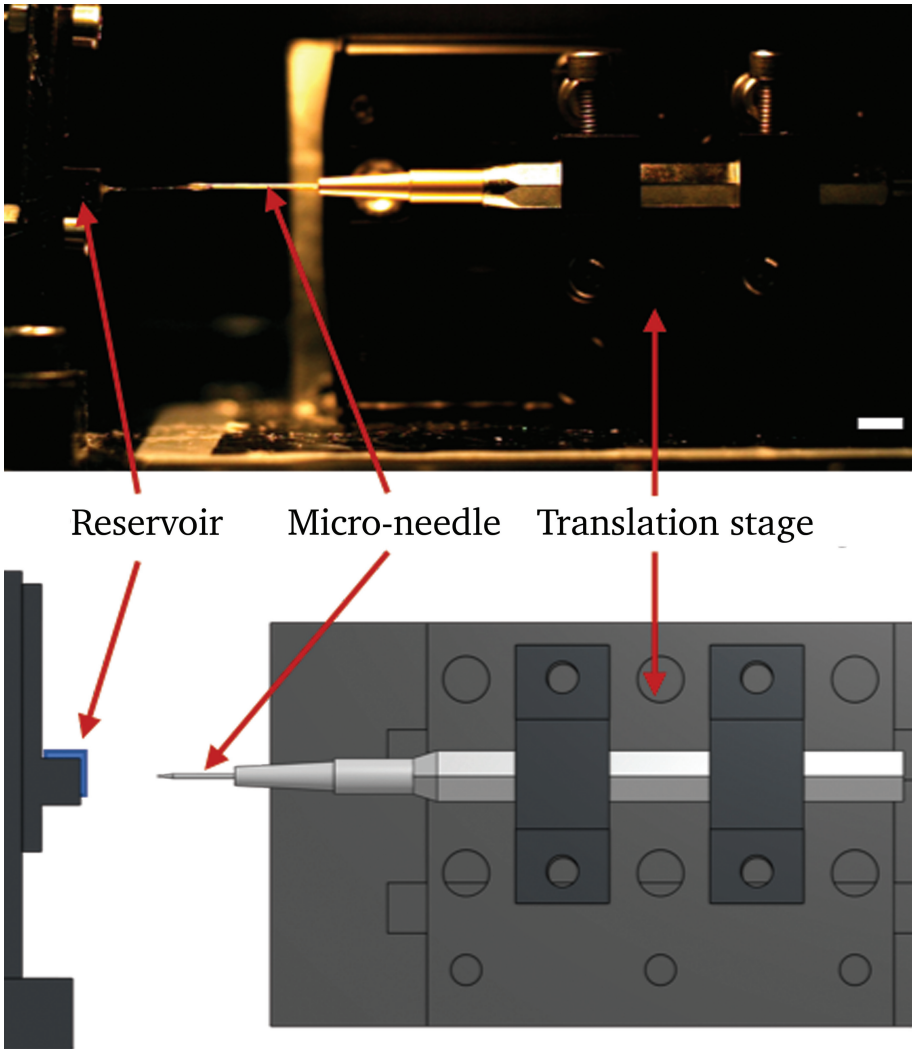

Figure 2.1: *Contact drawing system and accompanying schematic diagram. The system consists of a steel micro-needle mounted with 3D printed fittings onto a 100 mm translation stage. The polymer solution is held in the 50 µL 3D printed reservoir. The micro-needle can reach 4 mm deep into the reservoir. An Edgertronic high speed camera is used to take photos and videos of the contact drawing process. Scale bar = 10 mm.*

programmed in Kinesis). By measuring the time between the start and end of these 100 mm movements, the actual speed could be measured and is shown in Figure 2.2. The set speeds slower than 80 mm/s were calibrated at smaller incremental steps, to have more accuracy in the low velocity trials. In this study, the acceleration was always set to the maximum (5000 mm/s^2) and since the maximum speed was found to be approximately 400 mm/s, the set speed was always reached in 0.08 s or less. Therefore, we assumed fibre drawing occurred at constant velocities.

A reservoir for the polymer solutions was 3D printed. The reservoir was a $2 \times 5 \times 5$ mm rectangular prism (50 μL), with an open top and front face to allow filling with a syringe and the micro-needle to enter and draw fibres (see Figure A.2 for a drawing of the reservoir). This reservoir was mounted using 3D printed fittings so that the micro-needle could reach a depth of approximately 4 mm into the dextran solution (see Figure A.3 for a drawing of the mount). This was the depth used for all fibre drawing experiments.

The high speed camera was a constant part of the experimental setup, and was used to record videos of the fibre pulling process. These videos were later analyzed to understand key components of the fibre formation process, including the specifics

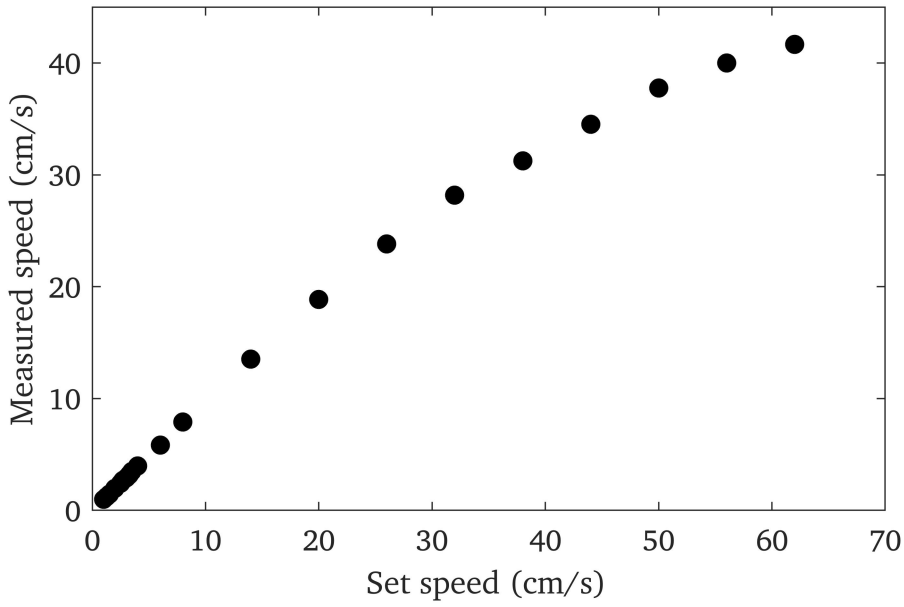

Figure 2.2: *The calibration curve obtained for the contact drawing setup. The set speed was programmed using the Kinesis software from Thorlabs, and the measured speed was obtained using high speed videos.*

of failure modes and the dynamics of the polymer solution near the reservoir.

2.3 Solution preparation

In this study, highly concentracted solutions of dextran were examined. The molecular weights (M_w) of dextran were: 70, 150, 250, and 500 kDa, as provided by the manufacturer. The 250 kDa dextran was purchased from Pharmacosmos and the 70, 150, and 500 kDa dextrans were purchased from Dextran Products Limited. For all failure analysis tests (section 2.4 below), Deionized (DI) water was used as the solvent. For the fibre diameter studies (section 2.5 below), both DI water and type I collagen in 0.02 N acetic acid (rat tail collagen I from Corning) were used as solvents.

To prepare a solution, the desired M_w dextran was selected, and the mass was measured in a plastic weighing dish. Then, the corresponding mass of solvent (DI water or collagen solution) was added to obtain the desired concentration (%wt dextran). The dextran and solvent were gently mixed together with a plastic pipette tip, until the solution appeared to be homogeneous. The solution was then transferred into a 1 mL syringe, to prevent evaporative loss of the solvent, and provide a simple way to fill the reservoir. The error on concentration was always less than 1 %wt, and can be attributed mainly to any evaporative loss of solvent, as quantified in Figure C.1.

The range of solution concentrations studied were approximately 40-50 %wt for 500 kDa dextran, 45-55 %wt for 250 kDa dextran, 53-58 %wt for 150 kDa dextran, and 59-64 %wt for 70 kDa dextran. At each M_w, the lower concentration limit was defined by the minimum at which fibre formation was observed, and the maximum was defined by a saturation limit, where the polymer could no longer be fully mixed into the solvent.

2.4 Failure analysis

To understand the mechanism of fibre formation, the contact drawing setup outlined in section 2.2 was used to study the parameters controlling successful fibre formation.

2.4.1 Experimental

Using a syringe, the liquid reservoir was filled with 50 μL of the desired dextran solution. The solution was replaced every 10 minutes to mitigate any effects of solvent evaporation (see Figure C.1), and to ensure that the volume of liquid in the reservoir was not depleted. Once filled, the stage was programmed to enter the reservoir at a speed of 29 mm/s to a depth of approximately 4 mm. At this depth the needle was stopped for 0.5 s, and then drawn at a controlled speed (v_{pull}) for the entire stage length; 100 mm. Thus, a pull duration (τ_{pull}) could be defined as:

$$\tau_{\text{pull}} = \frac{100\,mm}{v_{\text{pull}}}. \tag{2.1}$$

It is important to note that because the maximum acceleration time is 0.08 s, and the minimum τ_{pull} is 0.25 s, τ_{pull} was always much larger than the time needed to accelerate, and constant velocities over τ_{pull} were assumed.

During the pull step, it was observed whether a 100 mm fibre was formed, or if fibre formation failed before the stage travelled the full 100 mm path length. This observation was done by eye, using a bright LED lamp and a black backdrop. The set-up was well illuminated and the fibres scattered light, making them visible to a trained observer. Furthermore, when fibre formation failed, the free end would flail, making failure easy to spot. After each pull, the needle was cleaned with a Kimwipe soaked in ethanol.

In this study, two failure modes were observed. Mode I failures were termed relaxation failures, where a fibre was released from one or both ends before the pull step was complete. Mode II failures described trials where a droplet of solution was stranded on the fibre, and caused the fibre to droop and fall before the pull step was complete.

For a specific dextran solution (M_w and concentration), at least 15 trials were conducted at each τ_{pull}. From this, a failure rate could be determined as:

$$failure\,rate = \frac{\#\,of\;failed\,trials}{\#\,of\;total\,trials} \times 100\%. \tag{2.2}$$

In each set of trials, a minimum τ_{pull} was selected such that a 0% failure rate was observed. In corresponding sets, the τ_{pull} was incrementally increased until a 100% failure rate was observed.

2.4.2 Analysis

Using the MATLAB Curve Fitting Tool, the data for failure rate as a function of τ_{pull} were fit with a Weibull Cumulative Distribution Function (CDF) [65]. This function is defined as:

$$failure\,rate = 1 - exp\left[-\left(\frac{\tau_{\text{pull}}}{a}\right)^{k}\right] \tag{2.3}$$

where a is the scale parameter, and k is the shape parameter. Data sets were only fit if they had at least 3 failure rates that were not 0% or 100%. From these fits, the parameters a and k could be used to generate the corresponding Weibull probability density function (PDF):

$$\frac{d}{d\tau_{\text{pull}}}\left(failure\,rate\right) = \frac{k}{a}\left(\frac{\tau_{\text{pull}}}{a}\right)^{k-1} exp\left[-\left(\frac{\tau_{\text{pull}}}{a}\right)^{k}\right]. \tag{2.4}$$

The PDF was used to analyze the width of the distribution being fit, as the pre-factor $\frac{k}{a}$ played a critical role in determining the spread of the distribution.

2.5 Fibre diameter

This set of experiments was conducted to understand how the fibre diameter was controlled by τ_{pull}, dextran M_w, solution concentration, and choice of solvent. Due to the optics of the system, these diameters could not be measured during the pulling process. Instead, the fibres were collected on a glass slide and imaged afterwards.

2.5.1 Experimental

The first set of experiments characterized the relationship between fibre diameter and τ_{pull}. For these experiments, 3 solutions of 500 kDa dextran were made, at 42.5, 47.5 and 50.0 %wt dextran in water. Following the same steps as in subsection 2.4.1, these solutions were loaded into the reservoir, and a fibre was pulled at a desired τ_{pull}. This fibre was then collected on a $25 \times 75 \times 1$ mm glass slide (Ultident 170-7107A), with a 25 mm strip of double sided tape on each end. This was repeated until 5 fibres produced at the τ_{pull} were collected, and then this glass slide was capped by a $24 \times 50 \times 0.15$ mm glass coverslip (Deckgläser 470819). The capping layer helped keep the fibres attached to the glass slide, making them easier to image. Fibres were

collected at several τ_{pull} for each concentration, and then the fibres diameters were measured optically, as described in subsection 2.5.2 below.

For the second set of experiments, the relationship between fibre diameter and solution properties (dextran M_w and %wt dextran) were analyzed. For these experiments, 70, 150, 250, and 500 kDa dextrans were used at various concentrations of dextran. The fibres were created and collected in the same way as the first set of experiments, except that for all trials the τ_{pull} was fixed at 0.25 s. This low τ_{pull} allowed the broadest range of solutions to produce 100 mm fibres.

2.5.2 Analysis

The fibres were imaged using a Nikon Eclipse Ti optical microscope, fitted with a 40x objective. The fibres were imaged within a few hours of collection due to the hygroscopic nature of dextran, and its ability to absorb water from the air. Each fibre was imaged at 3 points, and each point was approximately 1 cm apart along the length of the fibre. These images were then imported into ImageJ. Once imported, the fibres were converted to binary, which made the edge of the fibre much more apparent. The binary images were processed by the ImageJ smooth function, which averaged the pixels in a 3x3 matrix. The smooth function removed the rough pixelated edges of the binary fibre, simplifying edge finding. Then, the fibre diameters were measured using the line tool in ImageJ, with a line width of 200 pixels. This process is shown in Figure 2.3. Using a wide line allowed each measurement to be an average over 17

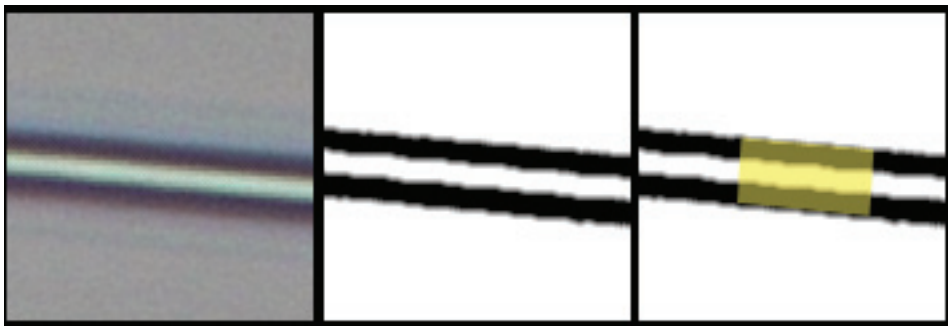

Figure 2.3: *Fibre diameters are measured using ImageJ. (a) The fibres are imaged using a Nikon optical microscope, and the images are imported into ImageJ. (b) The images are converted into binary, and processed using the smooth function. (c) On the processed images, the fibre diameter is measured using the line tool with a width of 200 pixels, or approximately 17 μm.*

μm of fibre length, and reduced error by ensuring the line was perpendicular to the fibre length.

Chapter 3

Results

3.1 Overview

To characterize the mechanism of fibre formation, the experimental apparatus from section 2.2 was used to draw liquid bridges. For a selected dextran solution, the needle was drawn at a speed such that a 10 cm liquid bridge was formed with 0% failure in at least 15 trials. In subsequent runs, the draw speed was decreased until a 100% failure rate was observed for at least 15 trials. To understand the fibre formation mechanism, these failure statistics were analyzed for 24 unique conditions. These conditions varied based on the dextran M_w and/or concentration. Dextrans of 70,

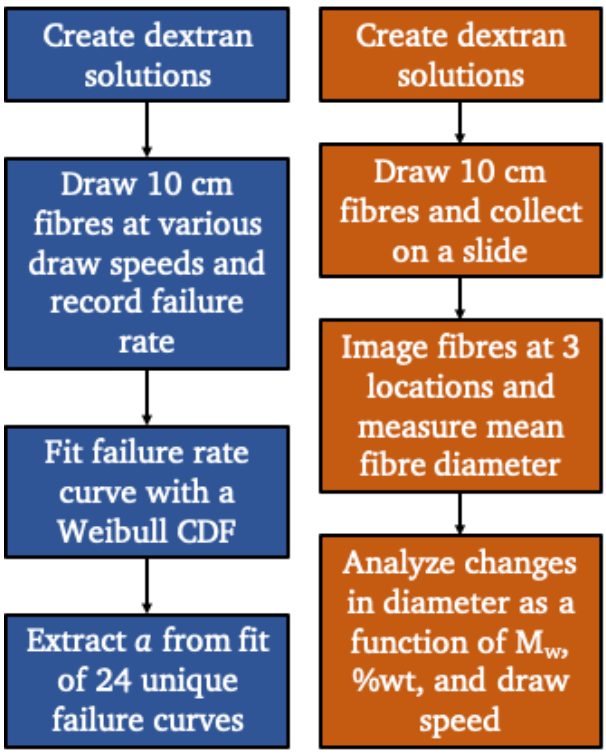

Figure 3.1: *An experimental flow chart, summarizing the fibre formation analysis experiments (blue), as well as the fibre diameter measurement experiments (orange).*

150, 250, and 500 kDa M_w were used, at concentrations between 58-63, 52-58, 45-55, and 40-50 %wt, respectively.

When a 10 cm liquid bridge was formed, it subsequently dried under ambient conditions creating a 10 cm long fibre. For a given τ_{pull}, dextran M_w, and dextran concentration, 5 fibres were collected and imaged at 3 locations. Using these 15 measurements, an average fibre diameter was calculated. This was done with 21 unique combinations of dextran M_w and concentration, 4 of which used collagen in acid as the solvent instead of deionized (DI) water. The fibre diameters ranged from 2-20 μm. Once dried, these fibres remained in this dry state for several months, with no signs of a long term relaxation. This experimental process is summarized in Figure 3.1.

3.2 Failure modes

The micro-needle was drawn from the solution reservoir, and as it travelled the 10 cm distance of the stage it elongated a liquid bridge of the dextran solution. In a sucessful trial, the liquid bridge was connected to both the micro-needle and to the liquid in the reservoir, for the entire τ_{pull}. As this elongation process continued, the liquid bridge dried under ambient conditions producing a fibre, which was still attached on both ends when the micro-needle came to rest. Failure was generally defined as an unsuccessful attempt to produce a 10 cm fibre, and two specific failure modes were observed, as illustrated in Figure 3.2.

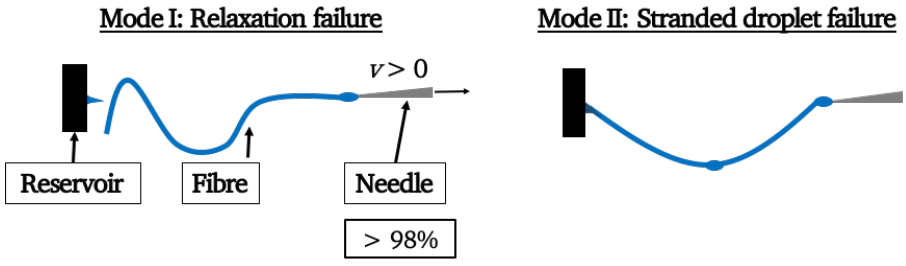

Figure 3.2: *Schematics showing the two failure modes observed in the failure analysis experiments. A relaxation failure defined trials where the fibre was no longer connected to the liquid reservoir and/or the micro-needle before the micro-needle came to rest. A stranded droplet failure defined a trial where a volume of liquid remained suspended along the length of the fibre, causing the fibre to droop and fall. Relaxation failures made up over 98% of the failures observed in this study.*

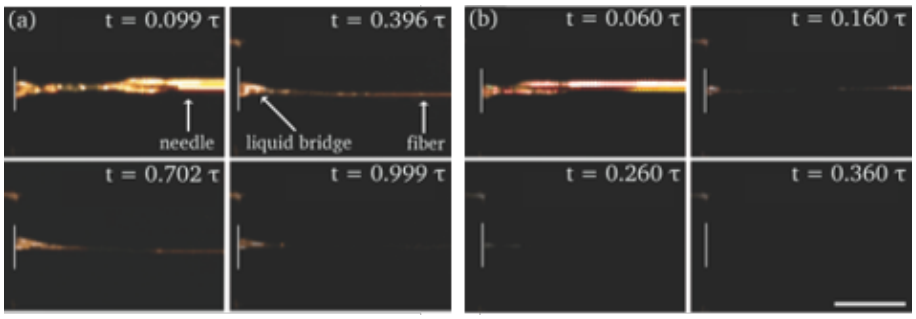

Figure 3.3: *Contact drawing of fibres from a 50 %wt solution of 500 kDa dextran and water. (a) A successful contact drawing process, where the fibre remains attached to the liquid reservoir throughout the entire τ_{pull} of 1.04s (left half). (b) A mode I failure, in which the liquid bridge is seen to be fully retracted into the liquid reservoir (bottom right panel) before $t = \tau_{pull} = 5.02s$. The white vertical lines highlight the front of the liquid reservoir. Scale bar = 5mm.*

More than 98% of the time, failure was categorized as a mode I relaxation failure. In a mode I failure, the fibre was released from either the liquid reservoir or the micro-needle before the micro-needle came to rest. With the fibres having diameters as large as 20 μm (section 3.4), they scattered light such that this failure mode was easily observable by eye for a trained observer. Figure 3.3 shows the prominence of this scattered light in both (a) a successful trial, and (b) a mode I failure. The stranded droplet failure (mode II) defined trials which failed due to a droplet of solution suspended along the length of the drying fibre. During the drawing process, the weight of this stranded droplet would cause the fibre to droop, and eventually fall onto the platform of the experimental apparatus before the micro-needle came to rest. This failure mode accounted for less than 2% of all failures observed. Since mode I failures were the most prominent, they were of the most interest when analyzing the mechanism for fibre formation.

3.3 Mode I failures and fibre formation

In characterizing fibre formation, sets of at least 15 trials were run at each τ_{pull}, and the ratio of failures to number of total trials defined the failure rate. Starting with a τ_{pull} that had a 0% failure rate, the τ_{pull} of corresponding experimentally sets was increased until a 100% failure rate was observed. This failure rate is shown in Figure 3.4 as a funtion of τ_{pull} for 4 different concentrations of 500 kDa dextran

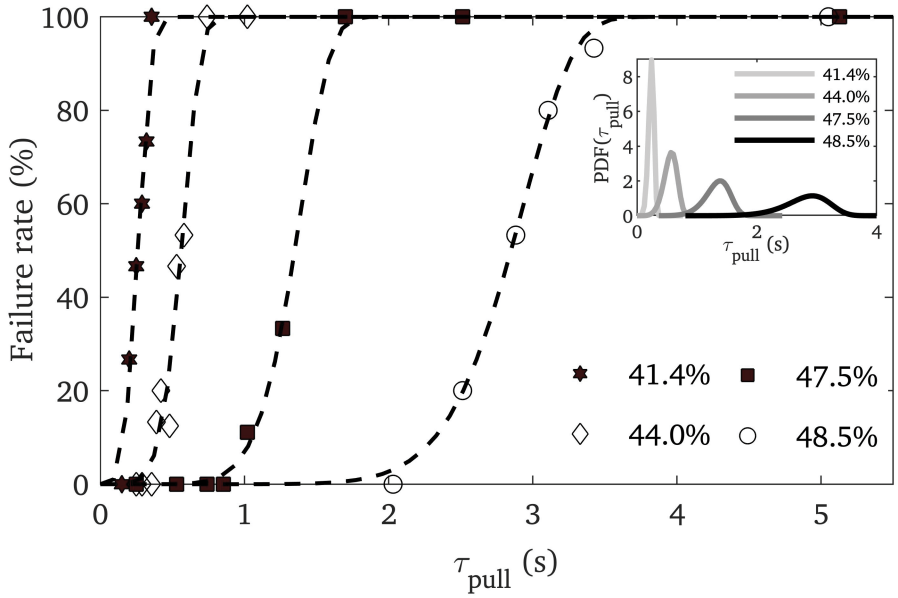

Figure 3.4: *Failure rate as a function of τ_{pull}, for 4 concentrations of 500 kDa dextran in water. Each data point is the failure rate calculated from at least 15 trials. Data sets are fit with a Weibull CDF (dashed lines, $r^2 > 0.9$). At each concentration, the failure rate undergoes a sharp transition from 0% to 100%. The scale parameter,* a *of the fitting function (Equation 2.3, characterizes a 63% failure rate, and can be extracted. The error on τ_{pull} is less than 1%. The inset graph shows the corresponding probability density function (Equation 2.4) for all 4 concentrations. As the concentration increases, the width of the distribution also increases.*

in water, where each of the data sets is fit with a Weibull Cumulative Distribution Function (CDF).

For each of the concentrations shown in Figure 3.4, the failure rate undergoes a sharp transition from 0% to 100% over a narrow range of τ_{pull}. The shape parameter of the Weibull fit, k, was found to be greater than 1 in all fits, describing a system where failure is guaranteed as time increases. The second model parameter, a, is the τ_{pull} corresponding to a 63% failure rate. Since the transition from 0% to 100% failure rate is extremely sharp, this model describes a system wherein a given solution is characterized by a critical timescale, and as τ_{pull} increases above that critical timescale, the system rapidly transitions from success modes to mode I failures. The τ_{pull} corresponding to these extracted a values were denoted τ_{exp}, and will be referred to as such from this point forward.

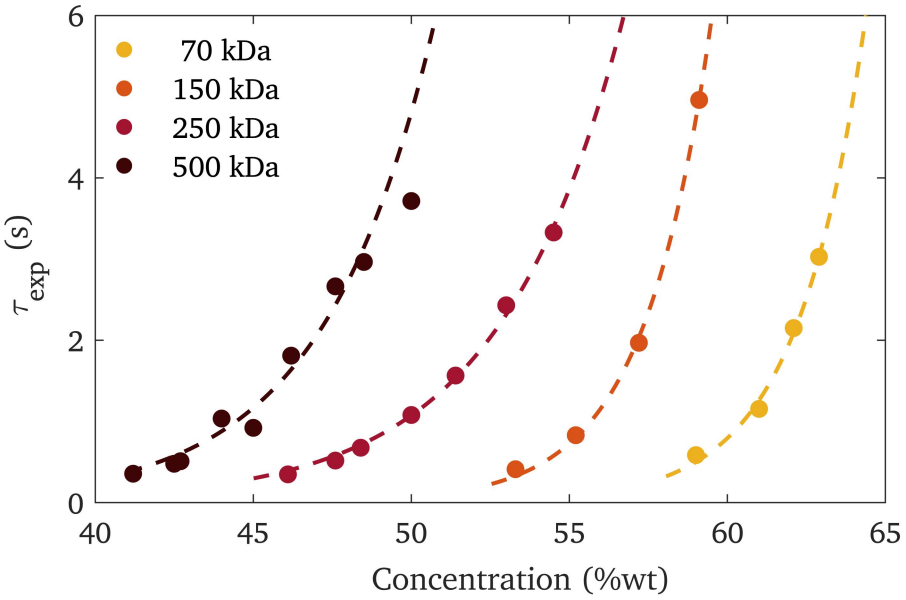

Figure 3.5: *τ_{exp} as a function of concentration for various M_w dextrans. τ_{exp} was determined as the scale parameter of the Weibull fits as shown in Figure 3.4. Each data set is fit with an exponential function (dashed lines, $r^2 > 0.9$). Error bars not shown, as the greatest error on τ_{exp} is 0.4s, and errors on concentration are less than 1 %wt.*

Using 70, 150, 250, and 500 kDa dextrans at various concentrations in water, a total of 24 data sets of failure rate as a function of τ_{pull} were obtained and fit, similarly to Figure 3.4. In these 24 data sets fit with a Weibull CDF, 19 data sets had an $r^2 > 0.90$, with the lowest $r^2 = 0.76$, showing the data was well represented by the Weibull model. Each fit had a $k > 1$, reaffirming that in every situation, the probability of failure increased as τ_{pull} increased, and was gauranteed to reach 100%. From all 24 fitted data sets, the τ_{exp} was extracted and plotted in Figure 3.5 as a function of dextran concentration.

For a given M_w, Figure 3.5 shows τ_{exp} increases with concentration, and is fit well with an exponential. Physically, this means that as the dextran concentration increases, the micro-needle can be drawn at a slower speed, thus at a higher τ_{pull}, while still successfully forming fibres. For all M_w dextrans, the range of τ_{exp} was very similar, and was found to be approximately 0.3 - 4.0 s. For a fixed concentration, τ_{exp} increases with M_w, as most clearly shown between the 250 and 500 kDa dextran data. The inset of Figure 3.4 shows the corresponding PDF for each concentration. As the concentration increases, the width of the PDF seems to increase, indicating

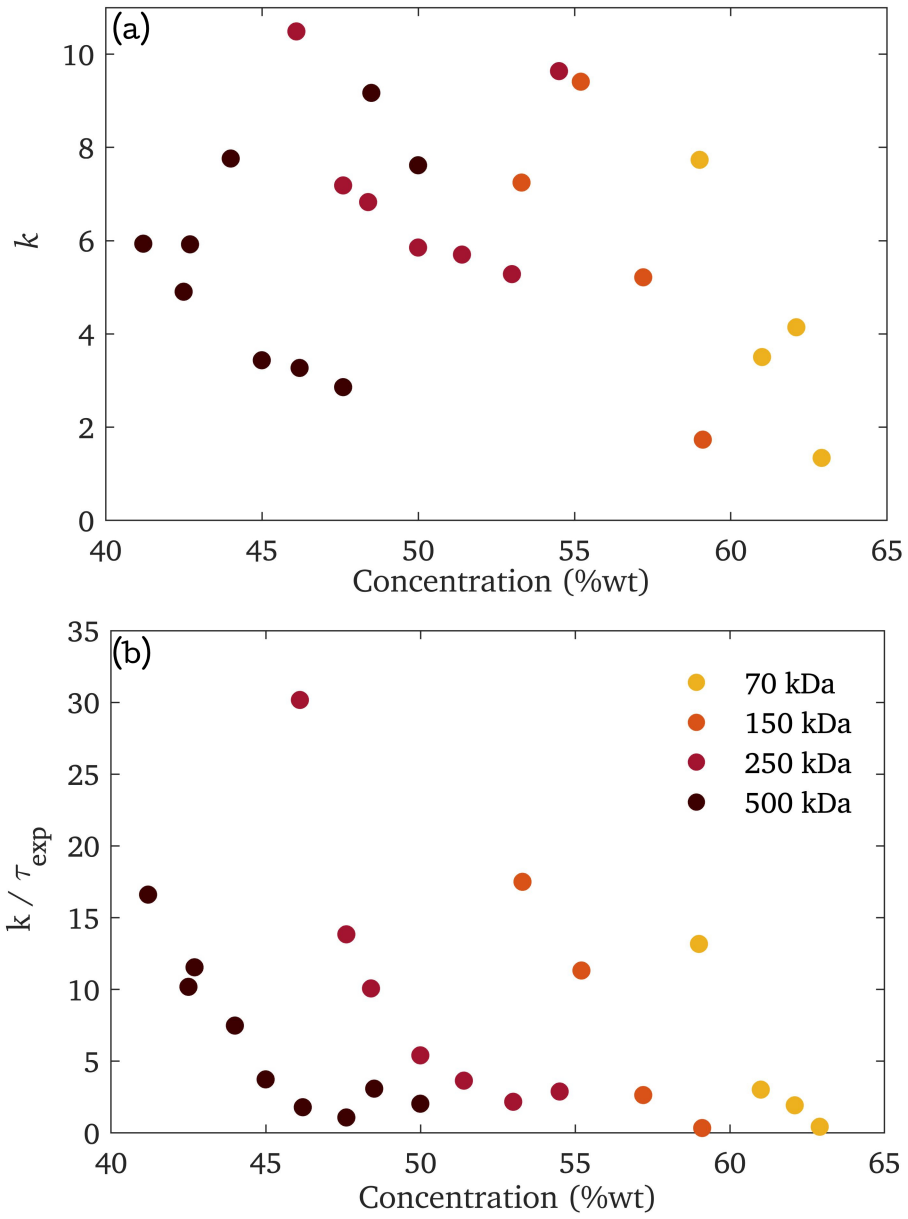

Figure 3.6: *(a) shows the shape parameter (k) as a function of concentration for 70, 150, 250, and 500 kDa dextrans. At each M_w, k tends to decrease with concentration. (b) shows the ratio, k/τ_{exp}, as a function of concentration for all 4 M_w. At each concentration, the ratio clearly decreases as the concentration increases. As k/τ_{exp} decreases, the width of the corresponding PDF would increase.*

that the range over which the transition to failure occurs gets broader with concentration. Based on Equation 2.4, the pre-factor $\frac{k}{a}$ plays a critical role in determining the amplitude of the peak in the PDF. Since the integral of each PDF must be 1, as the amplitude decreases, the width of the distribution must increase. The extracted

k from the 24 fits, and the ratios of $\frac{k}{\tau_{\text{exp}}}$ are shown in Figure 3.6, as a function of concentration.

Figure 3.6(a) generally shows a decrease in k as concentration increases, across all M_w dextrans. At a fixed τ_{exp} a decrease in k would result in a wider PDF, but since the τ_{exp} is changing with concentration, the ratio of k to τ_{exp} must be analyzed. This is shown in Figure 3.6(b), clearly demonstrating that the ratio decreases as concentration increases, across all M_w dextrans. Thus, as the concentration increases, the width of the corresponding PDF generally increases, suggesting a larger confidence interval of τ_{exp} values from the fit.

3.4 Fibre diameter

The first experimental set was focused on understanding how fibre diameter was dependent on τ_{pull}. Figure 3.7(a) shows the diameter as a function of τ_{pull} for 42.5,

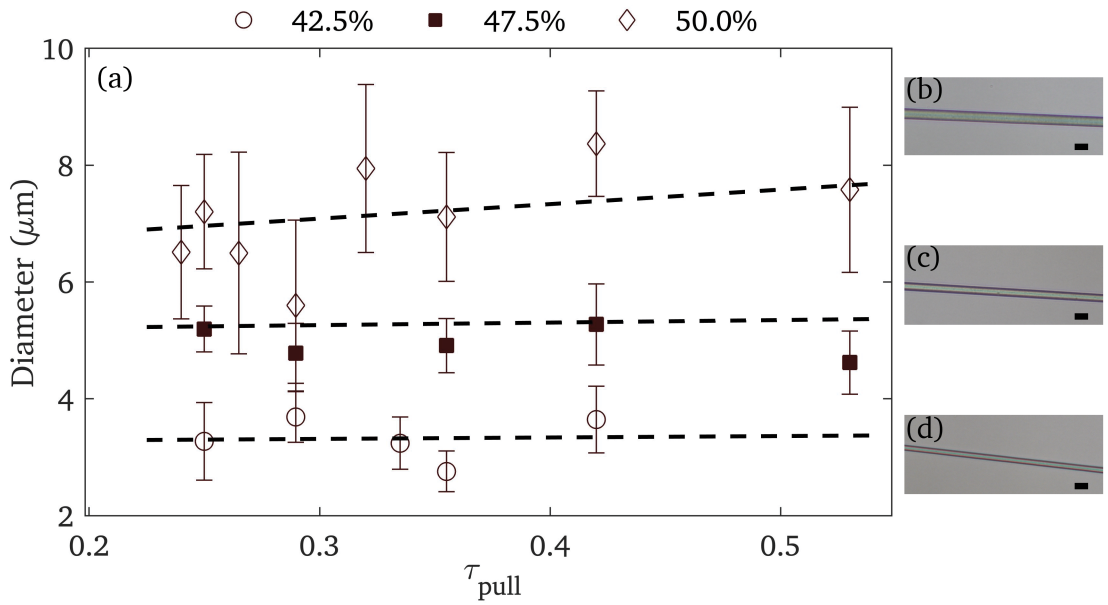

Figure 3.7: *Fibre diameter is shown as a function of τ_{pull} for 3 different concentrations of 500 kDa dextran in water. (a) Each fibre diameter data point is the average of 3 measurements on 5 fibres drawn under identical conditions. The fibre diameter remains constant with τ_{pull} (least squares fit, dashed lines), but increases with increasing dextran concentration (%wt, legend). Bars show the standard deviation of the average diameter measurement. Optical images of a fibre from the 50.0, 47.5 and 42.5 %wt solutions are shown in (b)-(d), respectively (scale bar = 10 μm). These optical images show a clear increase in fibre diameter with solution concentration.*

47.5, and 50.0 %wt solutions of 500 kDa dextran and water. The range of τ_{pull} in this experiment is from 0.25-0.55 s, because at longer τ_{pull} the 42.5 %wt solution would no longer form fibres. From Figure 3.7(a), it is clear that at each concentration, the fibre diameter is independent of τ_{pull}, within experimental variation. The error bars on the plot show the standard deviation of the average diameter, and this standard deviation is seen to increase with concentration, being the largest at 50.0 %wt. This figure also suggests the fibre diameter increases, with increasing concentration, as supported by the optical images in Figure 3.7(b)-(d).

With this result, the next experimental set was designed to understand the relationship between solution properties and fibre diameter. For these experiments, the fibre length was always 10 cm, and τ_{pull} was always 0.25 s. The results are shown in Figure 3.8, for 70, 150, 250, and 500 kDa dextrans. At each M_w, the diameter is seen to increase with concentration (exponential fit), while the overall range of diameters seems to be constant across the various dextrans. At a fixed concentration,

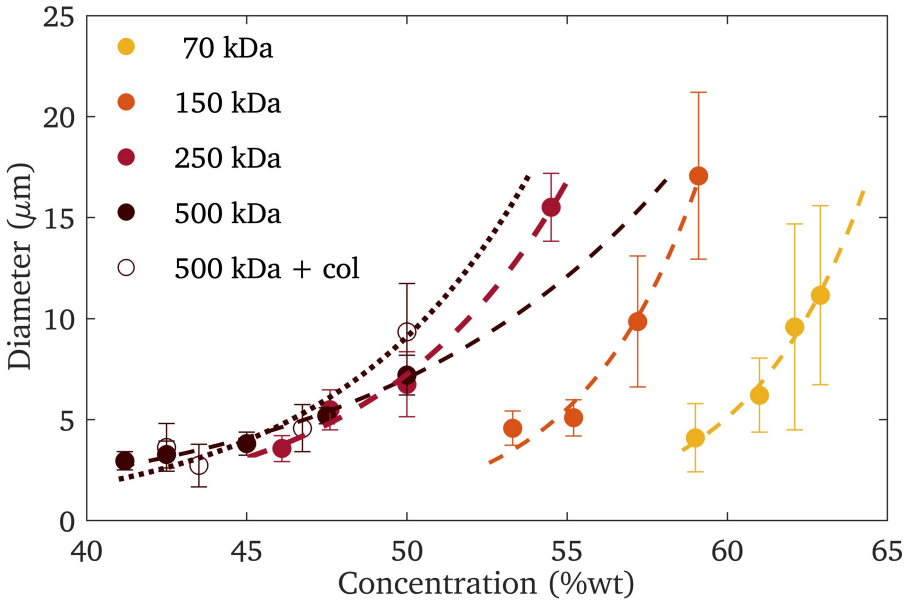

Figure 3.8: *Fibre diameter as a function of concentration for 4 different M_w dextrans. All of the fibres were 10 cm long, and the τ_{pull} was 0.25s. The diameter data points are the mean of 3 measurements on at least 5 fibres drawn under identical conditions. At each M_w, the fibre diameter scales with concentration (exponential fit, dashed line). This is also true for the 500 kDa + col fibres, where dextran was dissolved in a collagen solution instead of DI water. Error bars represent the standard deviation of the mean.*

the diameter generally increases with M_w, as most clearly seen between the 70, 150,

and 250 kDa dextrans. The open circles in Figure 3.8 show fibre diameters of 500 kDa dextran dissolved in a 8.7 mg/ml solution of collagen in acid. These data points overlap the 500 kDa dextran in water data well, indicating that a small incorporation of biological material does not impact the fibre formation. This suggests that the dextran plays the main role in both fibre formation and diameter tunability. Similar to Figure 3.7, this graph also shows an increase in the standard deviation with concentration, as seen at each M_w, suggesting that the variance in diameters is likely to have a concentration dependence.

3.5 Key findings

With over 360 trials characterizing failure of fibre formation, and over 100 fibre diameters measured, it is necessary to highlight the key results. Figure 3.4 showed that at each concentration, the failure rate sharply transitioned from 0% to 100% over a short range of τ_{pull}. These data were fit with Equation 2.3, and the scale parameters were extracted as τ_{exp}. These τ_{exp} values defined a characteristic timescale for each solution, such that at τ_{pull} less than τ_{exp}, fibre formation was likely to be successful, and as τ_{pull} increased, the probability of failure would also increase. When τ_{exp} was analyzed as a function of solution properties in Figure 3.5, τ_{exp} was found to increase with concentration (exponential fit), and was also seen to increase with M_w at a fixed concentration.

For the fibre diameters, Figure 3.7 shows that fibre diameter was independent of τ_{pull}. However, when measured as a function of solution properties in Figure 3.8, diameter was seen to increase with concentration (exponential fit), and also seen to increase with M_w at a fixed concentration. The addition of a small amount of collagen did not have any measurable impact on the fibre diameters, showing that small amounts of biological materials can be incorporated while still predicting the fibre diameter.

In both the fibre formation and fibre diameter studies, variance was seen to depend on solution concentration. For the fibre formation studies, this was shown in Figure 3.6(b), which suggested the width of the corresponding PDF increased with increasing concentration, across all M_w dextrans. In the fibre diameter experiments, this was most clearly demonstrated in Figure 3.8, where the standard deviation on

the diameter measurements increases with concentration.

Chapter 4

Discussion

4.1 Mechanism of fibre formation

4.1.1 Entangled solutions

To understand the contact drawing process and the key parameters controlling fibre formation, τ_{pull} was varied and fibre formation was observed for various solutions of dextran in DI water. At a fixed concentration and M_w, Figure 3.3 showed that at low τ_{pull} fibre formation was successful, but as τ_{pull} was increased, mode I failure was observed. By conducting trials at incrementally increasing τ_{pull} for a variety of concentrations and M_w dextrans, data of the increasing failure rate as a function of τ_{pull} was obtained, as shown in Figure 3.4. Each data set was fit with a Weibull Cumulative Distribution Function (CDF), which allowed the extraction of a τ_{exp}, corresponding to a critical timescale defining the transition from success to failure. In over 98% of cases, the failure was a mode I: relaxation failure, in which the liquid bridge attaching the fibre by one of its ends fully retracted, and the fibre was released. Since this was the dominant failure mode, it will be the focus of this discussion.

Another interpretation of this transition from success to failure is that of an elastic response to a viscous response: an elastic response would define fibre formation, whereas a viscous response would define the relaxation failure. In order to illicit this viscoelastic behaviour, the dextran solutions must have concentrations high enough that they are in the entangled regime. Through small-angle x-ray scattering experiments, it is known that dextran forms random coils in water, meaning that water is a θ-solvent for dextran [66]. Previous studies have shown that for 70 and 500 kDa dextran in water, the overlap concentration (c^*) is 10.4 and 5.0 g/dL or 11.6 and 5.3 %wt, respectively [67]. Although a complete theoretical understanding of estimating the entanglement concentration (c_e) is lacking, a previous study using dynamic light scattering quantified the c_e of aqueous 500 kDa dextran solutions to be 19 %wt [68].

In the same study, McCurdy and coworkers calculated a c^* of 4.7 %wt, such that $c_e \sim 4c^*$. In this study, our concentrations are up to 5 (70 kDa) and 10 (500 kDa) times larger than c^* (from [67]) such that all solutions we investigated were likely to be in the entangled regime.

Based on reptation theory (see section 1.3 for a more detailed background), at polymer concentrations above c_e polymers form temporary entanglements, which relax on the characteristic timescale known as the reptation time (τ_{rep}) [42]. In this model, a linear polymer is trapped in a tube, wherein the tube is defined by all of the intersections between the linear polymer and other polymers in the solution [69]. Thus, the linear polymer cannot diffuse laterally through the other polymers, and therefore the diffusion of the linear polymer is limited to one-dimension, which is defined as the dimension of the tube. As this polymer diffuses, τ_{rep} defines the time it would take for the polymer to completely diffuse out of its current tube, into a new tube, defined by intersections with a different set of other polymers [70]. Therefore in interacting with the system, if the interaction time is significantly longer than τ_{rep}, entanglements within the polymer solution will be abandoned and a viscous response will be observed where the solution flows freely. Interactions with the system at timescales much shorter than τ_{rep} would cause the entanglements to act as temporary crosslinks and an elastic response would be observed. In the intermediary regime, where interaction times are close to τ_{rep}, a viscoelastic response is observed, where the polymer solution elastically stores some of the interaction energy via entanglements, and flows to dissipate the remaining energy.

4.1.2 Applying reptation theory to fibre formation

In this study, all of the dextran solutions had concentrations 5-10 times above c^*, suggesting they were in the entangled regime. Figure 3.4 shows time-dependent transitions between an elastic response (successful fibre formation) to a viscous response (mode I relaxation failure), representing a system where entanglements could be the main mechanism for fibre formation. This would suggest the τ_{exp} extracted from the Weibull fits could be an experimentally determined τ_{rep}. This equivalence also provides an explanation for the trends seen in Figure 3.5, namely the increase in τ_{exp}

with concentration at a fixed M_w, and the increase in τ_{exp} with M_w at a fixed concentration. At a fixed M_w, an increasing concentration would lead to an increase in the entanglement density [58]. Thus, each polymer would have to abandon a greater number of entanglements to flow freely, leading to an increase in the time necessary to do so (τ_{rep}). At a fixed concentration, Figure 3.5 showed an increase in τ_{exp} with M_w, most clearly seen between the 250 and 500 kDa dextrans. In this case, the entanglement density remains unchanged, but doubling the M_w is analogous to joining two polymers end-to-end. Thus, each polymer would have to escape twice as many entanglements to flow, explaining the increase in τ_{exp} observed. Thus, by assuming τ_{exp} is an experimentally determined τ_{rep} the trends of Figure 3.5 can be explained, supporting this equivalency.

In entangled solutions of neutral (without free charges) polymers in θ-solvents, reptation theory predicts a universal scaling according to:

$$\frac{\tau_{rep}}{{M_w}^3} \sim c^{7/3}, \tag{4.1}$$

where c is the concentration of polymer in solution [32]. Figure 4.1 shows the τ_{exp} from Figure 3.5 re-scaled with $M_w{}^{-3}$. This re-scaling collapses the data across all M_w and 2.5 decades of concentration, onto a single exponential trend. The fact that a universal trend can be achieved based on the reptation theory prediction supports the conclusions that entanglements are the main mechanism for fibre formation in contact drawing, and that τ_{exp} can be interpreted as an experimentally determined τ_{rep}.

Although limited studies on contact drawing exist, the role of entanglements in electrospinning of fibres is well known. When preparing the polymer spin dope for electrospinning, it is necessary to have polymer concentrations greater than c_e in order to successfully form fibres [71]. At lower concentrations, electrospinning does not form fibres but creates droplets instead, defining a droplet printing technique known as electrospraying [58]. Thus for electrospinning to successfully occur, entanglements are necessary to create a fibre, as they stabilize the extruded volume of liquid from breaking apart into droplets due to the Rayleigh instability [58]. These entanglements must have a τ_{rep} large enough that adequate evaporation of solvent can occur from the forming fibre, such that the fibre is essentially solid [72]. As the solvent rapidly evaporates from the fibre, studies show that these fibres form a highly concentrated

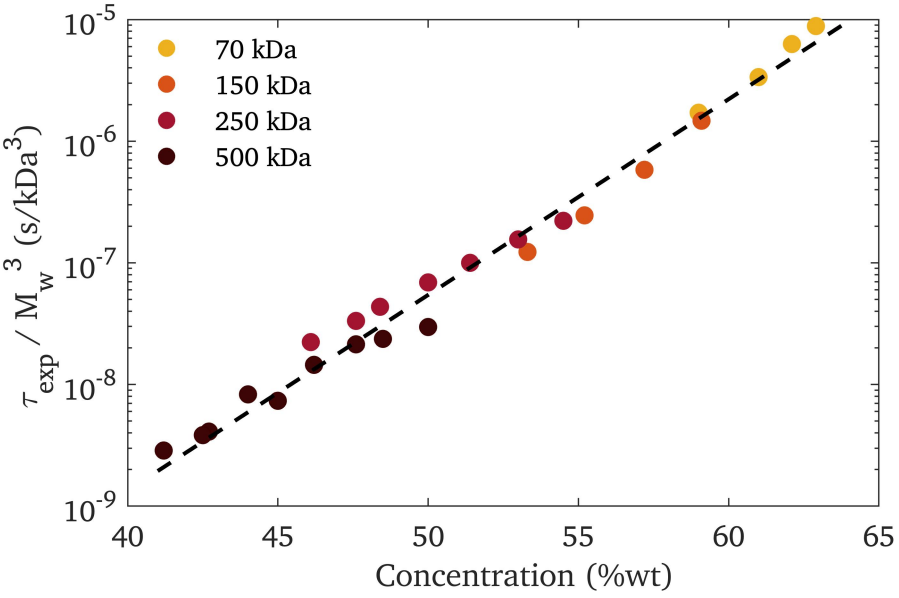

Figure 4.1: *A semi-log plot of τ_{exp} re-scaled as $\tau_{exp}/M_w{}^3$, as a function of concentration of dextran in solution. The data collapses on to a single universal exponential trend (dashed line, r^2 = 0.998). Error bars cannot but seen, but the largest error (90% tolerance) on τ_{rep} is 0.4 s at 500 kDa dextran. Errors on concentration are less than 1 %wt.*

shell structure, in which diffusion can no longer occur and therefore entanglements cannot relax [58]. Therefore, it would be expected that entanglements play a similar role in contact drawing where they stabilize the liquid bridge forming as the microneedle is drawn, and as the solvent rapidly evaporates diffusion is severely restricted, freezing the polymer structure within the formed fibre.

4.1.3 Deviations from reptation theory

Despite the fact that Figure 4.1 shows the data well fit (r^2=0.998) with an exponential, reptation theory predicts $\tau_{rep}/M_w{}^3$ to scale as a power law in concentration (Equation 4.1). However, reptation theory is based on monodisperse linear polymers, whereas the dextran is polydisperse (polydispersity index = 9.1 for 500 kDa dextran, per supplier), and is known to branch at high M_w [73, 74, 75]. Although presenting the dynamics of a polydisperse and branched polymer network is beyond the scope of this thesis, it is important to briefly discuss how these factors would impact the experimental results.

In reptation theory, a long chain linear polymer diffuses along a confined tube. The tube is defined by all of the points at which the polymer intersects other polymers in the solution, known as obstacles. If monodispersity is assumed, this tube can be treated as a fixed cage, because all obstacles would have the same relaxation time as the polymer of interest. Therefore, if an obstacle is to relax, it is equally likely for a new obstacle to appear, such that a fixed cage assumption is valid [41]. However, polydispersity does not allow for the fixed cage assumption, as obstacles of different lengths would have different relaxation times, creating a range of obstacle lifetimes. Obstacles defined by shorter polymers would relax earlier, decreasing the number of entanglements, and thereby increasing the diameter of the cage along which the polymer is diffusing [76]. Although this polydispersity does not inhibit reptation, it does indicate that a distribution of τ_{rep} is to be expected. This has been experimentally verified for aqueous dextran solutions with concentrations $> c^*$ using pulsed field gradient nuclear magnetic resonance to quantify the distribution of diffusion coefficients within a polydisperse dextran solution [77]. Compared to the range of diffusion coefficients that would be expected from independently testing all of the different molecular weights in the mass distribution, this study found a much narrower range of diffusion coefficients for the ensemble. This suggests a mechanism exists for ensemble averaging of the diffusion coefficients. Within an entangled solution, this averaging would be a direct result of reptation, as all polymers are connected through the entanglement network [77]. In the present study, the polydispersity index (PDI) is known for 500 kDa dextran to be 9.1 (as per manufacturer), which is significantly larger that the 1-3 PDI of the dextran used in [77]. This means that the polydispersity of at least the 500 kDa dextran used here is significant. Although studies have shown an ensemble averaging of relaxation times in polydisperse dextran solutions, the increased degree of polydispersity within this study would partially contribute to the width of the distributions in Figure 3.4.

High M_w dextrans are known to branch, which violates another major assumption of the reptation model. The assumption of a linear molecule allows a one-dimensional approximation of the molecule's diffusion through its tube. If a polymer is branched, reptation can be inhibited because the branched component of the polymer will also occupy an additional tube [78]. The tube of the polymer backbone and the branch

cannot be parallel, and therefore the polymer can no longer diffuse in one-dimension. However, for this to occur the length of the branched chain must be larger than the diameter of the tube through which the polymer is diffusing [77]. Although this has not be quantified in this study, the fact that reptation is occurring as supported by the observed relaxation failures, it is unlikely that there exists a large degree of long branched side chains. Within the limit that the branching does not inhibit reptation, it changes the polymer's configuration and would therefore have an effect on the dynamics of the polymer solution. If two molecules had the same M_w, but one was branched, the branched molecule would occupy a smaller pervaded volume than the linear molecule. Thus, at a fixed M_w, a solution of branched molecules would have a larger c^*, and therefore c_e, than a solution of linear molecules [79]. If the branched side chains are sufficiently short such that they do not inhibit reptation, as the solution concentration is increased well above c^*, entanglements will dominate the solution behaviour [38]. Therefore, these branched dextran molecules can be treated as shorter molecules, which would further contribute shorter times in the distribution of τ_{rep}.

In theory, a solution with a well known polymer concentration and M_w should have a well defined τ_{rep}. However, in this work we see that τ_{exp} has some distribution over τ_{pull} (Figure 3.4), defined by the fitting parameters of the Weibull fit (Figure 3.6). This is partially explained by the polydispersity and branching of the dextran, but variances in solution concentration would also have an effect on this. The concentration directly controls the entanglement density, which in turn controls τ_{rep}. Experimentally, mixing higher concentration solutions was harder as the dextran would not dissolve as well into the solvent. Since the distribution of the extracted τ_{exp} increases with concentration (seen in Figure 3.6(b)), and at increased concentrations solutions were less homogeneous, it is likely that local variances in solution concentration had a critical role in producing a broad distribution of τ_{exp} rather than a well-defined value. Despite the polydispersity of the dextran, any branching that may be present, and the variances in concentrations, the universal scaling achieved in Figure 4.1 shows that the reptation model is still applicable, supporting the assertion that entanglements play a critical role in fibre formation.

4.1.4 Weibull failure model

In proving the role of entanglements in fibre formation, and experimentally determining τ_{rep} for a variety of solutions, the Weibull model was used. The adoption of this model was motivated by two key factors. Firstly, it is a two-parameter model, where both parameters have physical analogues. The scale parameter, denoted τ_{exp} in these studies, defines the τ_{pull} corresponding to a 63% failure rate. Physically, this was interpreted as the critical timescale characterizing the transition from an elastic response to a viscous response. Although it is possible that using 63% failure rate rather than 50% could lead to an overestimation of τ_{rep}, Figure 3.3 shows that the failure rate increases rapidly, even at high concentrations, such that the difference in τ_{pull} at 50% compared to 63% is extremely small. This is further supported by the expected universal trend shown in Figure 4.1, which fits the τ_{exp} data almost perfectly ($r^2 = 0.998$). The shape parameter, k, described the width of the CDF, which represents the distribution of τ_{rep} in the dextran solutions. Since τ_{rep} has a concentration dependence, local variances in concentration would lead to variances in τ_{rep}, and this distribution would increase with increasing concentration, as shown in Figure 3.6(b). At higher concentrations, the solutions were less homogeneous due to difficulty in mixing, explaining the increased distribution characterized by k. Secondly, the Weibull model has been used extensively in the literature to study time-dependent failure, such as compressive failures in rock [80], fracture failures in fibres [81], and strength testing of dental materials [82]. This made physical interpretation of the parameters simple, as many studies focus on the details of both the scale parameter representing a time to failure, and the shape parameter representing the distribution of failure rate over time [83].

Although the τ_{rep} values extracted using the Weibull model fit the universal trend well (Figure 4.1), this success is not dependent on the choice of this specific model. In fact, many sigmoid functions would have worked just as well, as these functions define the 'S' shaped transitions observed in Figure 3.4, and allow control over the width of the distribution (k in the Weibull model) and the location of the curve along the x-axis (a in the Weibull model) [84]. Generally, the benefit of the Weibull model over sigmoid functions is that the Weibull function easily characterizes systems in which failure rate does not sharply transition to 100%, but this was never relevant

in this work. An even simpler route could be to take the average of the highest τ_{pull} corresponding to a 0% failure rate, and the lowest τ_{pull} corresponding to a 100% failure rate. The estimations for τ_{exp} from this approach are shown in Table 4.1 (average τ_{pull}), along with the actual τ_{exp} extracted from the Weibull function, for all of the concentrations studied with 500 kDa dextran. The average difference between the values was only -0.05 s, the average magnitude of difference was 0.16 s, and the largest difference was -0.42 s at 50 %wt. These differences tend to increase with concentration, which is expected due to increase in concentration variance at high concentrations, which is a key contributor to the distribution in τ_{rep} observed in this study. Since the values of an extremely arbitrary approach of averaging τ_{pull} yields similar results to τ_{exp} values extracted from the Weibull fits, it is unlikely that the choice of fitting model was critical to the experimental results found in this study.

Table 4.1: Comparing the τ_{exp} extracted from the Weibull model fits, to the average τ_{pull} between 0 and 100 % failure rate for each experimental set, for all data sets of 500 kDa dextran. The average difference between the Weibull parameter and the average τ_{pull} approach is -0.05 s, the average magnitude is 0.16 s, and the largest single difference is -0.42 s.

Concentration (%wt)	τ_{exp} from Weibull (s)	Average τ_{pull} (s)	Difference
41.2	0.36	0.27	0.09
42.5	0.48	0.46	-0.08
42.7	0.51	0.42	0.09
44.0	1.04	0.92	0.12
45.0	0.92	0.97	0.05
46.2	1.81	1.62	0.19
47.6	2.67	2.83	-0.16
48.5	2.96	3.17	-0.21
50.0	3.72	4.14	-0.42

4.2 Fibre diameters and secondary flows

4.2.1 Liquid bridge to polymeric fibre

In creating fibres, the first step was to load a solution with a known concentration and M_w into the reservoir. This solution was contacted with the micro-needle, and the micro-needle was then withdrawn 10 cm at a constant speed. As the micro-needle was

withdrawn, a small liquid bridge formed, which would elongate as the micro-needle travelled. During this elongation, solvent would evaporate from the liquid bridge creating a dry fibre along the central portion, replacing the liquid bridge. This now dry fibre was still connected to the micro-needle and liquid reservoir via liquid bridges that still existed at the ends. This defined two intersections between the solid fibre and liquid polymer solution. Once the needle came to rest, the liquid bridges would continue to flow towards their anchor (the liquid reservoir or the micro-needle), until a full 10 cm dry polymeric fibre was created. If kept in dry air, these fibres had long term stability and would remain solid for at least 8 months. Therefore, these fibres either dried completely, or had a dry polymeric shell that restricted any more solvent evaporation from the core of the fibre, which has been seen in other fibre manufacturing processes [58]. The final solvent content, or cross-sectional composition was never quantified in this study, but the fibres were seen to be stable for at least 8 months. This long term stability proves that the fibres were dry enough that diffusion of polymers no longer occurred at an observable timescale. However, dextran is known to be hygroscopic, and the water content of the fibre likely matched the humidity of the air they were kept in [85]. For this reason, fibre diameters were characterized immediately after fibre formation.

Within the fibre drawing process, the parameters that could control the fibre diameter would be the duration of pull (τ_{pull}), and the solution composition (dextran M_w and concentration). By drawing fibres at 3 concentrations of 500 kDa dextran in water at various τ_{pull}, it was observed that the fibre diameter was independent of τ_{pull} within variance (Figure 3.7). However, Figure 3.7 showed a clear increase in fibre diameter with solution concentration. In Figure 3.8, fibre diameters were measured across all 4 M_w dextrans, for a range of concentrations at $\tau_{\text{pull}} = 0.25$ s. These data also show a clear increase in fibre diameter with concentration at a fixed M_w, as well as an increase with M_w at a fixed concentration. Since τ_{pull} does not affect fibre diameter but the solution properties do, it is likely that fibre diameter is controlled during the flow process of the liquid bridges connecting the fibre by its ends, once the micro-needle has come to rest.

4.2.2 Secondary flow

To analyze this process, videos were recorded observing the flow of the liquid bridge back into the reservoir, as the bridge was still attached to the dry fibre. Timestamped images of this process are shown in Figure 4.2, for a (a) 45 %wt and (b) 50 %wt 500 kDa dextran solution. In both instances, the τ_{pull} was 0.25 s, and the first image (t = 0 s) was taken as the needle came to rest. The first frame of both (a) and (b) shows the characteristic liquid bridge profile of polymer solutions (as seen in Figure 1.3) with conical ends connected to a thin liquid cylinder. Figure 4.2 shows the last step of the fibre formation process, in which the conical end of the liquid bridge connecting the fibre to the liquid reservoir (clearly seen in Figure 4.2(b)) undergoes a secondary flow, until all of the liquid returns to the liquid reservoir. This secondary flow is driven by a recoverable elastic strain stored within the dextran solution [86, 87]. As the micro-needle elongates the dextran solution during the pulling process, the extended dextran chain configurations store a recoverable elastic energy. Similar to in a rubber, this elongated conformation of the polymers decreases their free energy, storing energy in the solution. Then, as these polymer chains begin to recoil, the secondary flow begins, during which this energy is recovered elastically as demonstrated by the retracting flow of the conical end. This stored elastic energy also explains how the liquid bridge

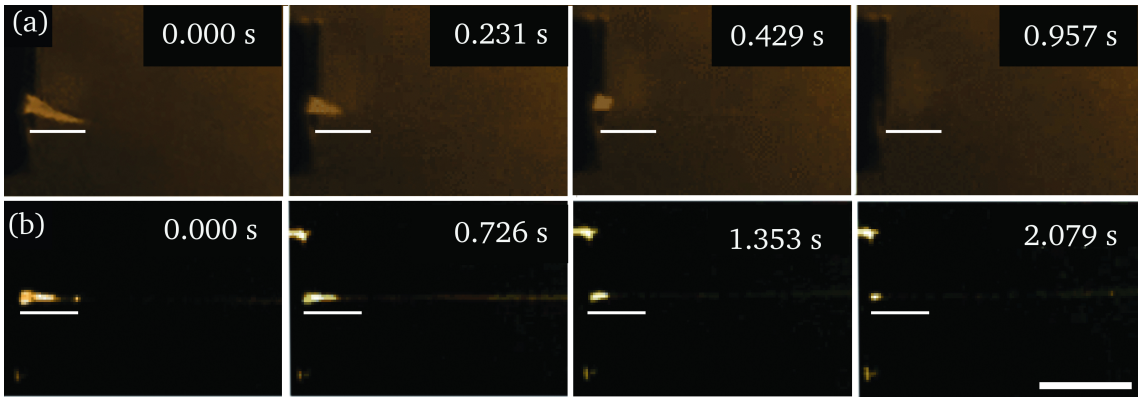

Figure 4.2: *The secondary flow after the stage has come to rest is shown in time stamped photos for (a) 45% and (b) 50% solutions of 500 kDa dextran in water. At t = 0 s, the fibre is attached to a liquid bridge, which through a secondary flow retracts into the reservoir and releases the fibre. At 45% this entire process occurred in less than 1 s, where as at 50% the process lasted more than 2 s. The white lines right below the liquid bridge show the length of the liquid bridge in the first frame of each series. Scale bar = 5 mm (bottom right).*

in Figure 4.2 (a) is able to climb upwards against gravity as it returns to the reservoir.

Interestingly, Figure 4.2 shows that the liquid bridge at 45 %wt flows back into the liquid reservoir more than twice as fast as the liquid bridge at 50 %wt, even though both formed over the same τ_{pull}. By tracking the tip of the conical end over time, an average speed of this secondary flow can be measured. At 45 %wt, the average flow speed was 3.1 mm/s, whereas at 50 %wt the average flow speed was only 1.1 mm/s. Thus, by analyzing the front of this necking region where the liquid bridge meets the solid fibre, a qualitative understanding of the trends in fibre diameter can be developed. Since all experiments occurred under ambient lab conditions (22.5 - 24.0 ^{o}C and at relative humidity less than 20%), a constant evaporation rate of solvent will be assumed for all fibres. With this assumption, a larger flow speed would result in a smaller fibre, because more polymer will be able to flow with the liquid bridge into the liquid reservoir, before the necessary volume of solvent has evaporated to fix the fibre diameter. Accordingly, at lower flow speeds, a larger fraction of the polymer remains in the fibre when the necessary volume of solvent has evaporated, resulting in a larger fibre diameter. In other words, by analyzing the conical tip of the liquid bridge, it is likely that the speed at which this secondary flow occurs controls fibre diameter. Since viscosity (η) is generally defined as a solution's resistance to flow [88], and Figure C.2 shows that the 45 %wt and 50 %wt solutions had a η of 8,000 cP and 85,000 cP, respectively, it then follows that η controls the speed of the secondary flow, which in turn controls the fibre diameter.

4.2.3 τ_{rep} as a proxy for η

To validate that η controls fibre diameter, the most compelling experiment would be analyzing the fibre diameter as a function of η. However, the falling ball method used to measure η requires extremely large volumes of solution, and thus was only performed for 500 kDa dextran solutions, meaning the data to show this plot does not exist. Nonetheless, by again using the reptation model it is possible to determine a scaling for η with our experimentally determined τ_{rep}. For entangled solutions of neutral polymers in θ-solvents, η is predicted as:

$$\eta - \eta_{\text{s}} \sim N^3 c^{14/3}, \tag{4.2}$$

where η_{s} is the solvent viscosity, N is the number of monomers in the polymer chain,

and c is the solute concentration within the solution [32]. Since the viscosity of the polymer solutions is 3-5 orders of magnitude larger than η_s ($\eta_{water} = 1$ cP),

$$\eta - \eta_s \approx \eta. \tag{4.3}$$

Equation 4.2 can then be rescaled to:

$$N^3 \sim \frac{\eta}{c^{14/3}}. \tag{4.4}$$

For neutral polymers in θ-solvents, reptation theory predicts that τ_{rep} scales as [32]:

$$\tau_{rep} \sim N^3 c^{7/3}. \tag{4.5}$$

Thus, substituting Equation 4.4 into Equation 4.5 yields:

$$\eta \sim \tau_{rep}\, c^{7/3}. \tag{4.6}$$

Equation 4.6 shows the theoretical scaling of η with τ_{rep} based on reptation theory. Figure 4.3 presents η (measured as per section C.2) as a function of $\tau_{exp}\, c^{7/3}$ for 500 kDa dextran in water. In this plot, η values were interpolated from Figure C.2. The

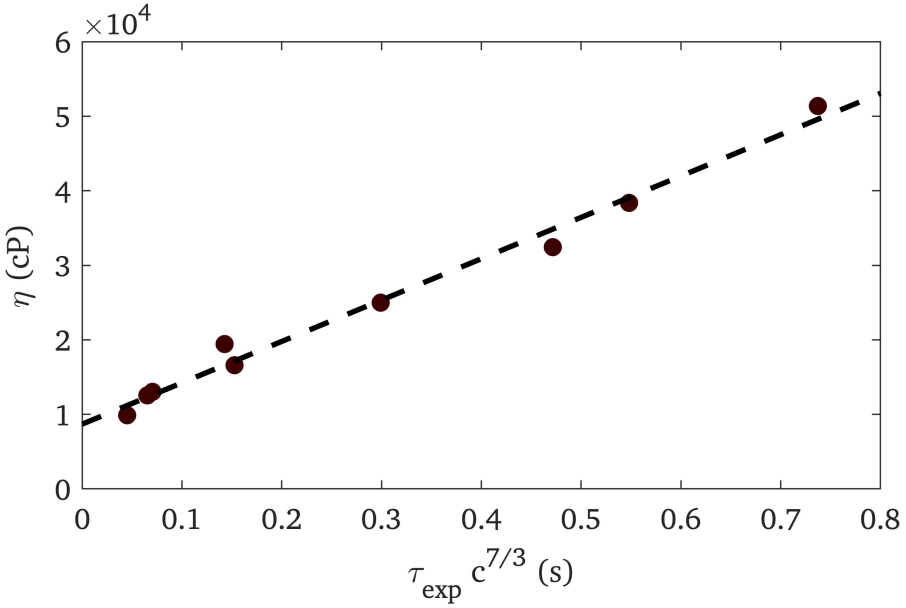

Figure 4.3: *η as a function of $\tau_{exp}\, c^{7/3}$ where c is the concentration of 500 kDa dextran in solution, shows a linear trend (dashed line, $r^2 = 0.99$). The η data is interpolated from Figure C.2.*

plot is well fit with a linear trend ($r^2 = 0.99$) as predicted by the reptation model. Therefore $\tau_{\text{exp}}\, c^{7/3}$ is a viable proxy of η.

With that, the fibre diameter data in Figure 3.8 can be re-scaled as a function of $\tau_{\text{exp}}\, c^{7/3}$. With this re-scaling, Figure 4.4 shows a linear trend of fibre diameter increasing as $\tau_{\text{exp}}\, c^{7/3}$ increases. Since $\tau_{\text{exp}}\, c^{7/3}$ is a proxy for η, these data show fibre diameter scales linearly with η across all M_w dextrans, even without a direct measurement of η. This further supports the earlier claim that the secondary flow is largely responsible for the fibre diameter, as an increasing η is responsible for a slower flow rate of the liquid bridge, which in turns leads to a larger fibre diameter. The increase in fibre diameter with concentration observed in Figure 3.8 can also be explained by the increase in concentration resulting in an increased η, and therefore a larger fibre diameter.

Electrospinning processes have also reported a larger fibre diameter with an increasing solution viscosity [79, 89]. In characterizing electrospun fibre diameters from entangled polymer solutions, these studies found that fibre diameter scaled as $\eta^{0.7-0.8}$, where η was the bulk viscosity of the solution. In a follow-on study it was found that it is the entanglement density of the solution that largely controls the fibre diameter

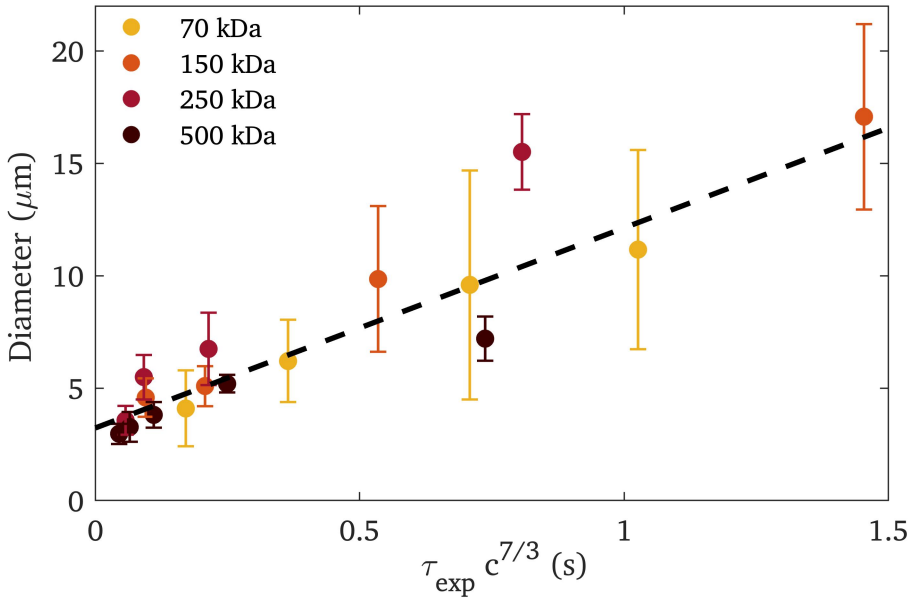

Figure 4.4: *Fibre diameter for various M_w dextrans as a function of $\tau_{exp}\, c^{7/3}$. $\tau_{exp}\, c^{7/3}$ serves as a proxy for η, and these data are fit with a linear trend (dashed line, $r^2 = 0.9$). The fibre diameter data was originally presented in Figure 3.8.*

[90]. In the electrospinning process, fibres are subjected to strain rates as high as 10^5 s^{-1} [91]. Thus as solvent is evaporating and a fibre is forming, it is being rapidly stretched. Since a fibre with a lower entanglement density would have a lower elastic modulus, this fibre would end up being thinner than a fibre with a higher entanglement density. Although the strain profile in the contact drawing process has not been characterized, an estimation of the maximum is certainly possible. In extension of liquid bridges, the strain rate is often quantified using the Hencky strain:

$$\dot{\epsilon} = \frac{2}{\Delta t} ln \left(\frac{R(0)}{R(t)} \right) \tag{4.7}$$

where $\dot{\epsilon}$ is the strain rate, Δt is the time over which the strain is applied, $R(0)$ is the initial radius of the liquid bridge, and R(t) is the radius of the liquid bridge at time = t [92]. From the present study, the shortest Δt is 0.25 s, the maximum $R(0)$ is the width of the reservoir (2 mm), and the smallest final radius is 1 μm. From these values, the maximum $\dot{\epsilon}$ can be estimated as 60 s^{-1}. This maximum strain rate is 4 orders of magnitude less than the strain rates in electrospinning. Therefore, the linear scaling of fibre diameter with η does not contradict this work, since contact drawn fibres are not subjected to the stretching process in electrospinning.

An interesting feature of Figure 3.8 is the increase in the standard deviation of the mean with an increase in concentration, at all M_w dextrans. A similar trend can be seen in Figure 4.4, where the standard deviation increases with $\tau_{rep}\, c^{7/3}$, at each M_w. Higher concentration solutions were more difficult to mix, resulting in more inconsistencies in concentration such as small amounts of undissolved dextran. Since the concentration controls the viscosity which in turn controls fibre diameter, these inconsistencies in concentration would lead to a distribution of fibre diameters. At higher concentrations, the number of inconsistencies were greater, and therefore the range of fibre diameters increased.

4.2.4 Diameters of collagen-containing fibres

For biomedical applications of these fibres (section 1.4), it was interesting to understand the contact drawing process with solutions containing biological material. In Figure 3.8, the open circles represent diameters of fibres formed from solutions of 500 kDa dextran dissolved in 8.7 mg/ml collagen in acid solution. These data overlap

the data for 500 kDa dextran in water well. Since the fibre diameters are controlled by solution viscosity, this suggests the use of collagen solution instead of water does not significantly change the viscosity of the solution. Furthermore, since the collagen would have a concentration of less than 0.5 %wt in the final solution, it is unlikely that the collagen would have any effect on the dynamics of the entangled dextran solution. In this case, the scaling in Figure 4.1 can be used to predict the conditions necessary to successfully form collagen/dextran fibres.

4.2.5 Bulk versus extensional viscosities

By analyzing the secondary flows, the final fibre diameter is found to scale linearly with solution viscosity. In determining this scaling, the viscosity was measured using the falling ball method, which is an excellent method for measuring the bulk viscosity (η) of a solution. However, in the work done here, the process of drawing long liquid bridges would involve applying extensional flows to the dextran solutions. In this case, the extensional viscosity (η_e) would be different from the bulk viscosity that was measured and used in the previous discussion.

η_e of entangled solutions is dependent on the strain rate ($\dot{\epsilon}$) [93, 94], which was defined in Equation 4.7. As $\dot{\epsilon}$ approaches zero, η_e approaches 3η as per the famous Trouton ratio [95]. Then, in entangled solutions as $\dot{\epsilon}$ increases, η_e decreases in the process known as shear thinning. This is due to the alignment of polymers that occurs as the polymers are strained, decreasing their resistance to flow [94]. The end of this early strain regime is defined by the point at which the individual polymer chains begin to stretch. From this point on, as $\dot{\epsilon}$ increases, η_e sharply increases beyond η, due to the stretching of individual polymer chains [94].

To determine η_e it is necessary to know the profile of $\dot{\epsilon}$. However, in this study constant speeds were applied, which translate into complex $\dot{\epsilon}$ profiles. To further complicate matters, as the fibre dries it is no longer strained in the same way as the liquid bridges. This non-uniform straining creates additional difficulties in translating the speed of the micro-needle to a $\dot{\epsilon}$ profile. In order to fully understand the effect of viscosity on fibre diameter it would be necessary to characterize $\dot{\epsilon}$ and therefore η_e throughout the fibre formation process.

Another factor contributing to η_e is the strain history of the solution. Since the entangled dextran solution can store elastic energy, the handling of the solution prior to creating fibres could also have an effect on η_e. As the dextran solution is mixed together, loaded into the syringe, extruded into the liquid reservoir, and strained by the micro-needle between pulls, the solution can store elastic energy. Previous studies have shown that pre-stretching of a polymer solution can increase η_e by up to 3-4 orders of magnitude [96, 97]. With no experimental control for 'resting' the polymer solution in the liquid reservoir after being extruded from the syringe and between pulls, the history of the polymer solution is likely to have an effect on η_e, and therefore the fibre diameters.

With the understanding that η_e is the best way to characterize viscosity in this study, the ideal plot would be the fibre diameter as a function of the average extensional viscosity over the pull duration. However, from this discussion it is obvious that η_e should scale with the bulk viscosity, likely as about 3 times larger. Therefore, the linear scaling in Figure 4.4 supports the assertion that solution viscosity largely controls fibre diameter.

Chapter 5

Conclusion

5.1 Summary of research outcomes

In this study, the characterization of polymeric fibres formed from stable liquid bridges during contact drawing was performed. Images of the necking region shown in Figure 4.2 resembled the shapes of the liquid bridges obtained in the methylcellulose studies [24], with defined conical ends connected by a thin cylindrical volume of liquid. However, the liquid bridges here stabilized at 10 cm length while being less than 20 μm in diameter, entering a new regime of liquid bridges where the lengths were at least 3 orders of magnitude greater than the radius. Due to the role of entanglements in stabilizing fibres during electrospinning [58], entanglements were proposed as the stabilizing mechanism in these liquid bridges. By characterizing the time-dependence of transition from successful fibre formation to the relaxation failures, the viscoelastic nature of the highly concentrated dextran solutions was characterized. More specifically, by fitting the failure rates for various dextran solutions, a critical timescale (τ_{exp}) could be extracted, which characterized the transition from fibre formation to failure. These extracted τ_{exp} values were excellently fit with a theoretical scaling of τ_{rep}, supporting the assertion that these extracted values may characterise the longest relaxation times of the entangled polymer solutions. As is true for electrospinning, polymer entanglements were largely responsible for stabilizing the liquid bridge as evaporation of the solvent occurred, and a final fibre was formed. Furthermore, the diameters of these final fibres were found to increase with solution viscosity, which is another similarity with electrospinning [90]. The mechanism however was different, as the flow rate of the secondary flows during the solvent evaporation was dependent on the viscosity, which in turn controlled fibre diameters in contact drawing. By applying concepts from liquid bridge stability, entangled polymer solutions, and electrospinning, we were able to characterize the formation and properties of fibres formed from contact drawing highly concentrated dextran solutions.

5.2 Significance

Contact drawing is a promising technique to produce collagen fibres for biomedical applications, as it is a highly scalable process requiring minimal specialized equipment, while preserving the collagen structure [1, 2]. As a result of this thesis work, the mechanism of fibre formation is now known which will be essential to optimizing the contact drawing process for the various applications. For example, if the universal scaling obtained in Figure 4.1 is extrapolated, it follows that by using longer linear polymers than 500 kDa dextran, the polymer concentration can be further decreased, thereby increasing the concentration of collagen in final fibres. This would be important for final applications in biomedicine, providing control over the concentration of fibre components.

Furthermore, by fitting the data in Figure 3.4, it was possible to extract a timescale that characterized the longest relaxation time of the polymer solution. Other methods to characterize this timescale require an experiment using small angle scattering of either neutrons or x-rays to determine the end-to-end radius of the polymer chain. From this radius the correlation length needs to be calculated. Then the diffusion is calculated in a different nuclear (or other) spectroscopic experiment, and by combining these findings the timescale corresponding to relaxation of entanglements can be found. In this study, obtaining one of the curves in Figure 3.4 to extract this relaxation time required less than 1 mL of polymer solution, and a linear translation stage. Although the extracted value was not as exact, the universal scaling suggests it is a fairly accurate characterization of τ_{rep}. Therefore, the horizontal micro-needle contact drawing system could have potential as a low-cost alternative to gauge the τ_{rep} of highly concentrated polymer solutions. As a characterization tool, this could have applications in electrospinning, wet-spinning and other fibre spinning techniques.

5.3 Further considerations

The data collected from these experiments certainly supports the assertion that polymer entanglements are responsible for fibre formation, and the solution viscosity plays a critical role in selecting the fibre diameter. In order to understand the contact drawing process completely, all relevant parameters must be controlled, which was

not always the case in these experiments. Here are a few of the key parameters that may have influenced the experimental results:

1. The volume of solution on the micro-needle, upon withdrawal from the liquid reservoir, was never characterized. It is likely that this volume plays a role in both fibre formation, and fibre diameter. It is possible that the solution closer to the needle is less likely to flow, due to the solid-liquid interface. Then it follows that at low volumes of liquid, this interface may have a greater effect on the flow of the liquid bridge, and therefore on fibre formation and fibre diameter. This parameter was not controlled, and could have contributed to the width of the Weibull functions, as well as the variance in fibre diameters.

2. The acceleration of the micro-needle. The linear stage used here had an acceleration phase. In the analysis, this acceleration phase was taken to be short enough that a constant velocity could be assumed, but at short times and short distances, this assumption would not be valid. Characterizing the acceleration more thoroughly would lead to better estimates of the extensional forces applied to the solution by the micro-needle. Since the elastic energy stored in the polymer solution plays a critical role in the secondary flow, which completes the fibre drawing process, characterizing the forces would lead to a more thorough analysis. The acceleration in these experiments was always set to the maximum, and was constant between experiments.

3. The humidity was not controlled in the lab. A critical part of the fibre formation process is the evaporation of the solvent. Since these experiments were all conducted under ambient conditions, the humidity in the lab would have an effect on the evaporation rate of the solvent. Although the evaporation was not shown to play a role in the success/failure of fibre formation, it likely plays a role in determining the fibre diameters. During the secondary flow, our analysis suggests that at larger viscosity, the solution would have a slower secondary flow, and a larger weight fraction of polymer would remain in the final fibre once the evaporation was complete. A change in evaporation rate would likely have an effect on this process. That being said, fibres collected for diameter measurements were all collected on the same day, so this is unlikely to contribute to the variance seen in the fibre diameter measurements.

5.4 Next steps

The purpose of science is to provide the knowledge to ask better questions. Here are a few research ideas that can be addressed in the future:

1. The experimental setup here was horizontal, but recreating a vertical system would be interesting. Unfortunately the stage used here could not generate the forces necessary for a vertical geometry. In a vertical system, the forces of gravity will likely play a larger role and would need to be included in the analysis. Gravity would lead to a more distorted shape of the forming liquid bridge, with a larger volume of solution towards the lower surface. This additional stress may allow 10 cm fibres to form at lower concentrations than those seen here. Furthermore, as seen in Appendix B it is possible that elastic rupture occurs during fibre formation which would be interesting to characterize. By designing a setup similar to the one used here, except with a stage capable of achieving high speeds in vertical motion, this experiment would be possible.

2. The inconsistency in concentration was a large source of error in this experiment, in both the fibre formation process, and the fibre diameters. This motivates the need for a more robust mixing protocol. One example could be mixing the solution using an automated device for a set amount of time, perhaps in a warmer water bath to help the mixing process. The solution can then be centrifuged to remove any gas bubbles, and brought back to room temperature. Repeating these experiments with more consistent concentrations could greatly reduce the variance observed.

3. These studies support the use of the extracted τ_{exp} as the τ_{rep} of the solution. To make this claim stronger, an interesting study would be to calculate τ_{rep} for a few of the concentrations. By using the traditional technique of measuring the end-to-end distance of the polymer, as well as the diffusion over time, this can be done. If this study were to confirm a correlation between τ_{exp} and τ_{rep}, the contact drawing setup developed here could be used as a simple and low-cost alternative to estimate the τ_{rep} of highly concentrated polymer solutions.

4. Performing these studies with other linear polymers that are of higher molecular weights, would be crucial to understanding how well the universal scaling of Figure 4.1 can be extrapolated. This is especially interesting because the universal scaling was achieved using the reptation model, which assumes perfectly linear and monodisperse

polymers which are not easily accessible at large molecular weights. By increasing the catalogue of polymers, the validity and limits of this scaling to be truly universal can be verified.

5. Expanding the characterization of final fibres beyond diameter would be interesting, and of high importance. By using methods such as x-ray diffraction, the molecular structure of the fibres can be quantified which would answer numerous questions important to final applications. For example, this would develop an understanding of polymer alignment within the final fibre, whether the polymer has a concentrated shell structure, what the distribution of biomolecules is within the fibre, and how all of these change with fibre manufacturing conditions and precursor solution properties.

6. Increasing the range of control parameters in the experimental apparatus would be very interesting. In these experiments, the micro-needle diameter, and the materials used were all kept constant. However, any effect the geometry of the needle has on fibre formation would be an interesting problem. The surface energy of any of the interfaces was also never considered. It could be possible, for example, that using a liquid reservoir that was more energetically favourable for the polymer solution would further increase the relaxation times. By characterizing these elements, it could be possible to increase the range of parameters that can be used as design inputs in an automated and scalable system.

Bibliography

[1] John P. Frampton, David Lai, Maxwell Lounds, Kyeongwoon Chung, Jinsang Kim, John F. Mansfield, and Shuichi Takayama. Elongation of fibers from highly viscous dextran solutions enables fabrication of rapidly dissolving drug carrying fabrics. *Adv. Healthcare Mater.*, 4(2):313–319, 2015.

[2] G. Y. Liu, R. Agarwal, K. R Ko, M. Ruthven, H. T. Sarhan, and J. P. Frampton. Templated assembly of collagen fibers directs cell growth in 2d and 3d. *Scientific Reports*, 7(1):9628, 2017.

[3] R. D. Gillette and D. C. Dyson. Stability of axisymmetric liquid-fluid interfaces towards general disturbances. *The Chemical Engineering Journal*, 3:196–199, 1972.

[4] David Megias-Alguacil and Ludwig J. Gauckler. Capillary forces between two solid spheres linked by a concave liquid bridge: Regions of existence and forces mapping. *AIChE Journal*, 55(5):1103–1109, 2009.

[5] Manu Prakash, David Quéré, and John W. M. Bush. Surface tension transport of prey by feeding shorebirds: The capillary ratchet. *Science*, 320(5878):931–934, 2008.

[6] Sijia Hu and Carolyn A. Koh. Interfacial properties and mechanisms dominating gas hydrate cohesion and adhesion in liquid and vapor hydrocarbon phases. *Langmuir*, 33(42):11299–11309, 10 2017.

[7] F. Soulié, F. Cherblanc, M.S. El Youssoufi, and C. Saix. Influence of liquid bridges on the mechanical behaviour of polydisperse granular materials. *International Journal for Numerical and Analytical Methods in Geomechanics*, 30(3):213–228, 2006.

[8] G. Walker. Adhesion to smooth surfaces by insects - a review. *International Journal of Adhesion and Adhesives*, 13(1):3–7, 1993.

[9] J. Qian and H. Gao. Scaling effects of wet adhesion in biological attachment systems. *Acta Biomaterialia*, 2:51–58, 2006.

[10] Gerrit Huber, Hubert Mantz, Ralph Spolenak, Klaus Mecke, Karin Jacobs, Stanislav N. Gorb, and Eduard Arzt. Evidence for capillarity contributions to gecko adhesion from single spatula nanomechanical measurements. *Proceedings of the National Academy of Sciences of the United States of America*, 102(45):16293–16296, 2005.

[11] Satish Kumar. Liquid transfer in printing processes: Liquid bridges with moving contact lines. *Annual Review of Fluid Mechanics*, 47(1):67–94, 2015.

[12] Thomas Young. An essay on the cohesion of fluids. *Philosophical Transactions of the Royal Society A*, 95:65 – 87, 1805.

[13] M.A Fortes. Axisymmetric liquid bridges between parallel plates. *Journal of Colloid and Interface Science*, 88(2):338 – 352, 1982.

[14] I. Martinez and J.M. Perales. Liquid bridge stability data. *Jounral of Crystal Growth*, 78:369–378, 1986.

[15] S. Gaudet, G. H. McKinley, and H. A. Stone. Extensional deformation of newtonian liquid bridges. *Physics of Fluids*, 8:2568–2579, 1996.

[16] Amir Akbari and Reghan J. Hill. Liquid-bridge stability and breakup on surfaces with contact-angle hysteresis. *Soft Matter*, 12:6868–6882, 2016.

[17] J Meseguer, L.A Slobozhanin, and J.M Perales. A review on the stability of liquid bridges. *Advances in Space Research*, 16(7):5 – 14, 1995. Microgravity Sciences: Results and Analysis of Recent Spaceflights.

[18] T.-Y. Chen, J. A. Tsamopoulos, and R. J. Good. Capillary bridges between parallel and non-parallel surfaces and their stability. *Journal of Colloid and Interface Science*, 151(1):49–69, June 1992.

[19] J. Plateau. *Statique Expérimentale et Théoretique des Liquides Soumis aux Seules Forces Moléculaires*, volume 2. Gauthier Villars, 1873.

[20] Brian James Lowry and Paul H. Steen. Capillary surfaces: Stability from families of equilibria with application to the liquid bridge. *Proceedings: Mathematical and Physical Sciences*, 449(1937):411–439, 1995.

[21] Yakov I. Rabinovich, Madhavan S. Esayanur, and Brij M. Moudgil. Capillary forces between two spheres with a fixed volume liquid bridge: Theory and experiment. *Langmuir*, 21(24):10992–10997, 11 2005.

[22] Zongfu Dai and Shouci Lu. Liquid bridge rupture distance criterion between spheres. *International Journal of Mineral Processing*, 53(3):171 – 181, 1998.

[23] Jinda Zhuang and Sungtaek Ju. A combined experimental and numerical modeling study of the deformation and rupture of axisymmetric liquid bridges under coaxial stretching. *Langmuir*, 31(37):10173–10182, 2015.

[24] Svetlana Morozova, Peter W. Schmidt, Athena Metaxas, Frank S. Bates, Timothy P. Lodge, and Cari S. Dutcher. Extensional flow behavior of methylcellulose solutions containing fibrils. *ACS Macro Letters*, 7(3):347–352, 2018.

[25] A. V. Bazilevsky, V. M. Entov, and A. N. Rozhkov. *Liquid filament microrheometer and some of its applications*. Elsevier, New York, 1990.

[26] G. H. McKinley and A. Tripathi. How to extract the newtonian viscosity from capillary breakup measurements in a filament rheometer. *Journal of Rheology*, 44(3):653–670, 2000.

[27] Gareth H. McKinley and Tamarapu Sridhar. Filament-stretching rheometry of complex fluids. *Annual Review of Fluid Mechanics*, 34(1):375–415, 2002.

[28] P. J. Flory. Thermodynamics of high polymer solutions. *The Journal of Chemical Physics*, 9:660–661, 1941.

[29] P. E. Rouse. A theory of the linear viscoelastic properties of dilute solutions of coiling polymers. *The Journal of Chemical Physics*, 21:1272, 1953.

[30] R. A. L. Jones. *Soft condensed matter*. Oxford University Press, 2014.

[31] Izumi Nishio, Shao-Tang Sun, Gerald Swislow, and Toyoichi Tanaka. First observation of the coil–globule transition in a single polymer chain. *Nature*, 281(5728):208–209, 1979.

[32] Ralph H. Colby. Structure and linear viscoelasticity of flexible polymer solutions: Comparison of polyelectrolyte and neutral polymer solutions. *Rheologica Acta*, 49(5):425–442, 5 2010.

[33] P. G. DeGennes. Dynamics of entangled polymer solutions. i. the rouse model. *Macromolecules*, 9(4):587–593, 1976.

[34] P. G. DeGennes. *Scaling Concepts in Polymer Physics*. Cornell University Press, 1979.

[35] G. Astarita. Therodynamics of dissipative amterials with entropic elasticity. *Polymer engineering and Sceince*, 14(10):730–733, 1974.

[36] John D. Ferry. *Viscoelastic properties of polymers*. John Wiley & Sons, 1980.

[37] M. A. Valdez and J. Tejero. Hydrodynamic interactions of dilute polymer solutions under shear flow in a narrow channel. *Rheologica Acta*, 33:125–135, 1994.

[38] W. Graessley. Polymer chain dimensions and the dependence of viscoeleastic properties on concentration, molecular weight and solvent power. *Polymer*, 21(3):258–262, March 1980.

[39] V. Bertola. Dynamic wetting of dilute polymer solutions: The case of impacting droplets. *Advances in Colloid and Interface Science*, 193-194:1 – 11, 2013.

[40] M. Muthukumar and S. F. Edwards. Screening concepts in polymer solution dynamics. *Polymer*, 23(3):345–38, 1982.

[41] Masao Doi and S. F. Edwards. Dynamics of concentrated polymer systems. part 1.—brownian motion in the equilibrium state. *Journal of the Chemical Society, Faraday Transactions 2: Molecular and Chemical Physics*, 74:1789–1801, 1978.

[42] P. G. de Gennes. Reptation of a polymer chain in the presence of fixed obstacles. *The Journal of Chemical Physics*, 55(2):572–579, 1971.

[43] Jan Skov Pedersen and Peter Schurtenberger. Scattering functions of semidilute solutions of polymers in a good solvent. *Journal of Polymer Science Part B: Polymer Physics*, 42(17):3081–3094, 2004.

[44] U. K. Chaturvedi, U. Steiner, O. Zak, G. Krausch, G. Schatz, and J. Klein. Structure at polymer interfaces determined by high-resolution nuclear reaction analysis. *Applied Physics Letters*, 56(13):1228–1230, 1990.

[45] G. Reiter and U. Steiner. Measurements of polymer diffusion over small distances. a check of reptation arguments. *Journal de Physique II*, 1(6):659–671, 1991.

[46] Fabián Vaca Chávez and Kay Saalwächter. Time-domain nmr observation of entangled polymer dynamics: Universal behavior of flexible homopolymers and applicability of the tube model. *Macromolecules*, 44(6):1549–1559, 03 2011.

[47] K. Adachi, T. Wada, T. Kawamoto, and T. Kotaka. Dielectric spectroscopy on dilute blends of polyisoprene/polybutadiene: Effects of matrix polybutadiene on the dynamics of probe polyisoprene. *Macromolecules*, 28:3588–3596, 1995.

[48] TT Perkins, DE Smith, and S Chu. Direct observation of tube-like motion of a single polymer chain. *Science*, 264(5160):819–822, 1994.

[49] R. F. Liang and M. R. Mackley. Rheological characterization of the time and strain dependence for polyisobutylene solutions. *Journal of Non-Newtonian Fluid Mechanics*, 52(3):387–405, 1994.

[50] K. Gelse, E. Poschl, and T. Aigner. Collagens - structure, function and biosynthesis. *Advanced Drug Delivery Reviews*, 55(12):1531–1546, 2003.

[51] M. Shoulders and R. Raines. Collagen structure and stability. *Annual Review of Biochemistry*, 78(1):929–958, 2009.

[52] Cilla Söderhäll, Ingo Marenholz, Tamara Kerscher, Franz Rüschendorf, Jorge Esparza-Gordillo, Margitta Worm, Christoph Gruber, Gabriele Mayr, Mario Albrecht, Klaus Rohde, Herbert Schulz, Ulrich Wahn, Norbert Hubner, and Young-Ae Lee. Variants in a novel epidermal collagen gene (col29a1) are associated with atopic dermatitis. *PLOS Biology*, 5(9):1–10, 09 2007.

[53] Z. Huang, Y. Zhang, M. Kotaki, and S. Ramakrishna. A review on polymer nanofibers by electrospinning and their applications in nanocomposites. *Composites Science and Technology*, 63(15):2223–2253, 2003.

[54] Bogdan Cramariuc, Radu Cramariuc, Roxana Scarlet, Liliana Rozemarie Manea, Iuliana G. Lupu, and Oana Cramariuc. Fiber diameter in electrospinning process. *Journal of Electrostatics*, 71(3):189 – 198, 2013.

[55] Geoffrey Ingram Taylor. Disintegration of water drops in an electric field. *Proceedings of the Royal Society of London. Series A. Mathematical and Physical Sciences*, 280(1382):383–397, 1964.

[56] D.H. Reneker, A.L. Yarin, H. Fong, and S. Koombhongse. Bending instability of electrically charged liquid jets of polymer solutions in electrospinning. *Journal of Applied Physics*, 87(9 I):4531–4547, 2000. cited By 1969.

[57] Y. M. Shin, M. M. Hohman, M. P. Brenner, and G. C. Rutledge. Electrospinning: A whipping fluid jet generates submicron polymer fibers. *Applied Physics Letters*, 78(8):1149–1151, 2001.

[58] Suresh L. Shenoy, W. Douglas Bates, Harry L. Frisch, and Gary E. Wnek. Role of chain entanglements on fiber formation during electrospinning of polymer solutions: good solvent, non-specific polymer–polymer interaction limit. *Polymer*, 46(10):3372 – 3384, 2005.

[59] J. Matthews, G. Wnek, D. Simpson, and G. Bowlin. Electrospinning of collagen nanofibers. *Biomacromolecules*, 3(2):232–238, 2002.

[60] W. Teo and S. Ramakrishna. Electrospun fibre bundle made of aligned nanofibres over two fixed points. *Nanotechnology*, 16(9):1878–1884, 2005.

[61] Dimitrios I. Zeugolis, Shih T. Khew, Elijah S.Y. Yew, Andrew K. Ekaputra, Yen W. Tong, Lin-Yue L. Yung, Dietmar W. Hutmacher, Colin Sheppard, and Michael Raghunath. Electro-spinning of pure collagen nano-fibres – just an expensive way to make gelatin? *Biomaterials*, 29(15):2293 – 2305, 2008.

[62] Jochen Bürck, Stefan Heissler, Udo Geckle, Mohammad Fotouhi Ardakani, Reinhard Schneider, Anne S. Ulrich, and Murat Kazanci. Resemblance of electrospun collagen nanofibers to their native structure. *Langmuir*, 29(5):1562–1572, 2013. PMID: 23256459.

[63] G. D. Pins, D. L. Christiansen, R. Patel, and F. H. Silver. Self-assembly of collagen fibers. influence of fibrillar alignment and decorin on mechanical properties. *Biophysical Journal*, 73:2164–2172, October 1997.

[64] Jeffrey M. Caves, Vivek A. Kumar, Jing Wen, Wanxing Cui, Adam Martinez, Robert Apkarian, Julie E. Coats, Keith Berland, and Elliot L. Chaikof. Fibrillogenesis in continuously spun synthetic collagen fiber. *Journal of Biomedical Materials Research*, 93B(1):24–38, 2010.

[65] P.L Hall and J.E Strutt. Probabilistic physics-of-failure models for component reliabilities using monte carlo simulation and weibull analysis: a parametric study. *Reliability Engineering & System Safety*, 80(3):233 – 242, 2003.

[66] Eleftheria Antoniou, Efrosyni Themistou, Biswajit Sarkar, Marina Tsianou, and Paschalis Alexandridis. Structure and dynamics of dextran in binary mixtures of a good and a bad solvent. *Colloid and Polymer Science*, 288(12):1301–1312, 2010.

[67] Eleftheria Antoniou and Marina Tsianou. Solution properties of dextran in water and in formamide. *Journal of Applied Polymer Science*, 125(3):1681–1692, 2012.

[68] R. D. McCurdy, H. D. Goff, D. W. Stanley, and A. P. Stone. Rheological properties of dextran related to food applications. *Food Hydrocolloids*, 8(6):609–623, 1994.

[69] S F Edwards. The statistical mechanics of polymerized material. *Proceedings of the Physical Society*, 92(1):9–16, sep 1967.

[70] PG de Gennes. Entangled polymers. *Physics Today*, 36(6):33–39, June 1983.

[71] El-Refaie Kenawy, John M. Layman, Jessica R. Watkins, Gary L. Bowlin, Jamil A. Matthews, David G. Simpson, and Gary E. Wnek. Electro-spinning of poly(ethylene-co-vinyl alcohol) fibers. *Biomaterials*, 24:907–913, September 2003.

[72] Zeming Gou and Anthony J. McHugh. Two-dimensional modeling of dry spinning of polymer fibers. *Journal of Non-Newtonian Fluid Mechanics*, 118:121–136, 2004.

[73] Rifat Z. Ahmed, Khaizran Siddiqui, Muhammad Arman, and Nuzhat Ahmed. Characterization of high molecular weight dextran produced by weissella cibaria cmgdex3. *Carbohydrate Polymers*, 90:441–446, May 2012.

[74] Arthur J. Ragauskas, Siwames Netsopa, Suwanna Niamsanit, Duangkamon Sakloetsakun, and Nipa Milintawisamai. Characterization and rheological behavior of dextran from weissella confusa r003. *International Journal of Polymer Science*, 2018.

[75] Catalina E. Ioan, Thomas Aberle, and Walther Burchard. Light scattering and viscosity behavior of dextran in semidilute solution. *Macromolecules*, 34(2):326–336, 01 2001.

[76] G. Marrucci. Relaxation by reptation and tube enlargement: A model for polydisperse polymers. *Journal of Polymer Science: Polymer Physics Edition*, 23(1):159–177, 1985.

[77] P. T. Callaghan and D. N. Pinder. A pulsed field gradient nmr study of self-diffusion in a polydisperse polymer system: Dextran in water. *Macromolecules*, 16(6):968–973, 1983.

[78] William W. Graessley. *Entangled linear, branched and network polymer systems — Molecular theories*. Springer Berlin Heidelberg, Berlin, Heidelberg, 1982.

[79] Matthew G. McKee, Garth L. Wilkes, Ralph. H. Colby, and Timothy E. Long. Correlations of solution rheology with electrospun fiber formation of linear and branched polyesters. *Macromolecules*, 37(5):1760–1767, 03 2004.

[80] Teng fong Wong, Robina H.C. Wong, K.T. Chau, and C.A. Tang. Microcrack statistics, weibull distribution and micromechanical modeling of compressive failure in rock. *Mechanics of Materials*, 38(7):664 – 681, 2006.

[81] M. Sutcu. Weibull statistics applied to fiber failure in ceramic composites and work of fracture. *Acta Metallurgica*, 37(2):651 – 661, 1989.

[82] Janet B. Quinn and George D. Quinn. A practical and systematic review of weibull statistics for reporting strengths of dental materials. *Dental Materials*, 26(2):135 – 147, 2010.

[83] R. Jiang and D.N.P. Murthy. A study of weibull shape parameter: Properties and significance. *Reliability Engineering & System Safety*, 96(12):1619 – 1626, 2011.

[84] Tomás Jónás. Sigmoid functions in reliability based management. *Social and Management Sciences*, 15(2):67–72, Feb 2007.

[85] A Jeanes, C A Wilham, and J C Miers. Preparation and characterization of dextran from leuconostoc mesenteroides. *Journal of Biological Chemistry*, 176(2):603–615, Nov 1948.

[86] A. Ya. Malkin and C. J. S. Petrie. Some conditions for rupture of polymer liquids in extension. *Journal of Rheology*, 41(1):1–25, 1997.

[87] Y. M. Joshi and M. M. Denn. *Rheology Reviews 2004*, chapter Failure and Recovery of Entangled Polymer Melts in Elongational Flow, pages 1–17. The British Society of Rheology, Aberystwyth, Wales, 2004.

[88] S. P. Sutera and R. Skalak. The history of poiseuille's law. *Annual Reviews - Fluid Mechanics*, 25:1–19, 1993.

[89] Pankaj Gupta, Casey Elkins, Timothy E. Long, and Garth L. Wilkes. Electrospinning of linear homopolymers of poly(methyl methacrylate): exploring relationships between fiber formation, viscosity, molecular weight and concentration in a good solvent. *Polymer*, 46(13):4799 – 4810, 2005.

[90] Chi Wang, Yu Wang, and Takeji Hashimoto. Impact of entanglement density on solution electrospinning: A phenomenological model for fiber diameter. *Macromolecules*, 49(20):7985–7996, 10 2016.

[91] A. Greiner and J. H. Wendorff. Electrospinning: A fascinating method for the preparation of ultrathin fibers. *Angewandte Chemie*, 46:5670–5703, 2007.

[92] G. H. McKinley. Visco-elasto-capillary thinning and break-up of complex fluids. *Annual Rheology Reviews*, pages 1–49, 2005.

[93] Christopher J.S. Petrie. One hundred years of extensional flow. *Journal of Non-Newtonian Fluid Mechanics*, 137(1):1 – 14, 2006.

[94] P. K. Bhattacharjee, J. P. Oberhauser, G. H. McKinley, L. G. Leal, and T. Sridhar. Extensional rheometry of entangled solutions. *Macromolecules*, 35(27):10131–10148, 12 2002.

[95] F. T. Trouton. On the coefficient of viscous traction and its relation to that of viscosity. *Proceedings of the Royal Society A*, 77:426–440, May 1906.

[96] R. I. Tanner. Stresses in dilute solutions of bead-nonlinear-spring macromolecules. iii. friction coefficient varying with dumbbell extension. *Transactions of the Society of Rheology*, 19(557-582), 1975.

[97] Charles M. Schroeder, Hazen P. Babcock, Eric S. G. Shaqfeh, and Steven Chu. Observation of polymer conformation hysteresis in extensional flow. *Science*, 301(5639):1515–1519, 2003.

Appendix A

CAD Drawings

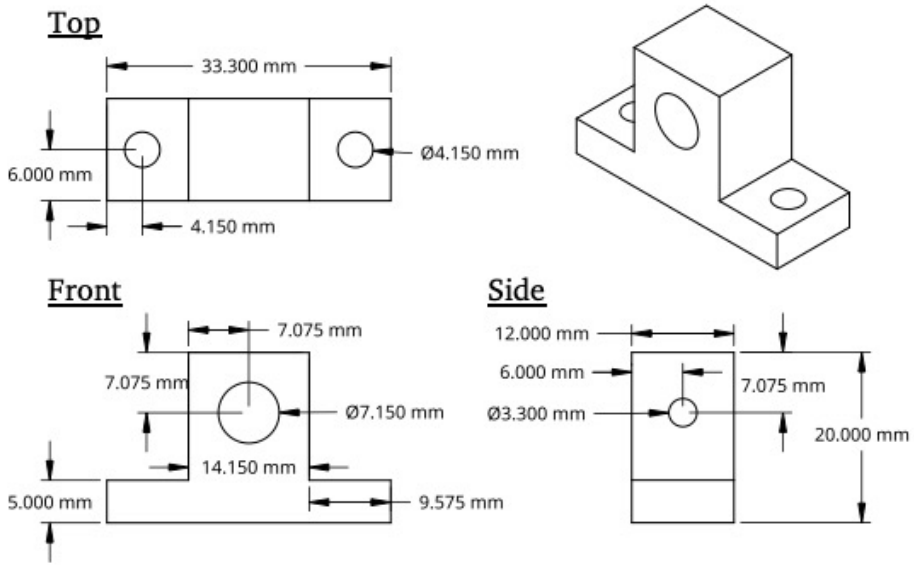

Figure A.1: *This drawing shows the 3D printed piece for mounting the micro-needle holder. Two of these pieces were printed and screwed into the translation stage. The micro-needle was mounted into the holder, and the holder was slid into the large hole on the front, and fixed in place with set screws. Scale 2:1.*

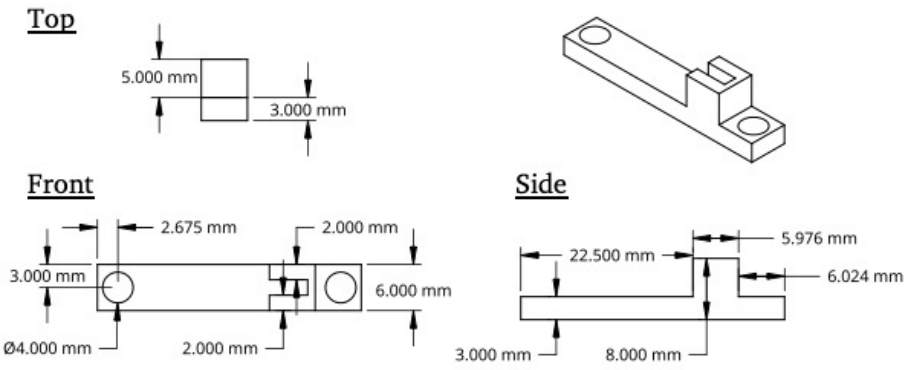

Figure A.2: *This drawing shows the 3D printed liquid reservoir. This reservoir has a volume of 50 μL, and was filled with the polymer solution during the contact drawing experiments. Scale 2:1.*

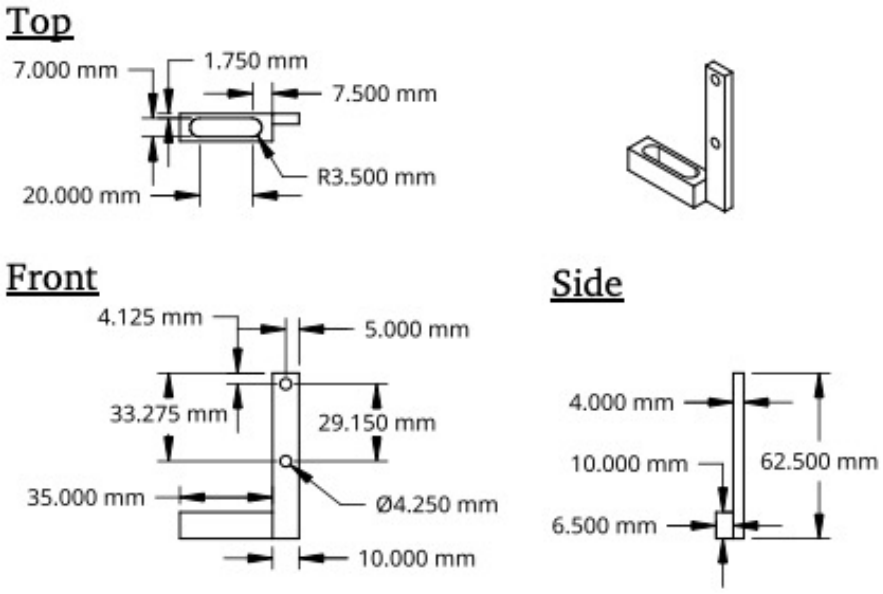

Figure A.3: *This drawing shows the 3D printed mount for the reservoir (Figure A.2). The holes on the front face of the reservoir were screwed into the two holes on the front face of this mount. Scale 1:2.*

Appendix B

Preliminary Experiment

A preliminary experiment was conducted, which greatly informed the experiments described in this thesis. In this experiment, a 50 %wt solution of 500 kDa dextran in water was created. This solution was then used to form a drop on a glass slide. The micro-needle was mounted onto a handle, and using the handle the micro-needle was manually dipped into the puddle and pulled away. This was done approximately 40 times, and each of these trials was recorded using the high speed camera described in section 2.2.

For each trial, it was observed whether a fibre formed, whether no fibre formed, or whether a "limited fibre" formed, in which a fibre either relaxed or elastically ruptured. Using the videos from the high speed camera, a pull speed for each trial could be measured, which was approximated as the average velocity over the first 5 cm. Since there was no control for the evaporation of solvent from the droplet, the time elapsed since solution preparation was recorded.

The data in Figure B.1 shows some important features which were used to inform the experimental design of this study. Time elapsed measures the time since the solution preparation, and can be used as a proxy of evaporation. As the time elapsed increases, the concentration of dextran in water also increases, until a highly concentrated 'shell' is formed on the exterior of the droplet.

At early time points before 10 minutes (regime I), there is a clear change in fibre formation as a result of pull speed. During this time where the dextran concentration is lowest, as the pull speed increases, a change from limited fibres to successful fibre formation is observed. At intermediary time points (regime II), the dextran concentration is increased, and even at lower pull speeds fibre formation is observed. At late time points (regime III), the dextran concentration has increased further, and fibre failure is frequently observed. In this late time regime, failure was attributed to occurrences of the needle not starting a fibre, or a fibre that elastically ruptured, as

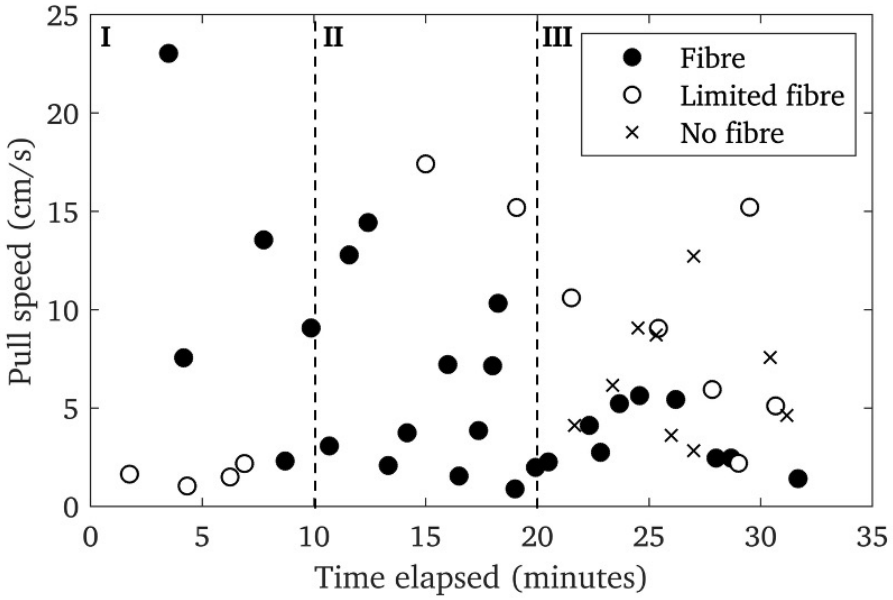

Figure B.1: *This figure shows the preliminary data that informed the experimental design described in this study. The data can be segmented into 3 time regimes: I) early, II) intermediary, and III) late. As time goes on, the dextran concentration in the solution droplet increases.*

observed from the high speed videos.

Although this was not a thorough experiment, these results were informative in arriving at the final study. Firstly, this experiment showed the importance of controlling for evaporative loss. The fact that failure at a fixed pull speed changed with time elapsed, shows that the concentration is crucial in understanding this process, and thus evaporative loss would need to be controlled. In order to further understand how the evaporative loss occurs, see Figure C.1. Furthermore, as is most clearly demonstrated in the first 10 minutes of Figure B.1, at a fixed concentration, pull speed likely has an effect on fibre formation. This result suggested the existence of a critical timescale for the fibre formation process.

Appendix C

Solution Characterization

The rate of evaporation and bulk viscosity were measured for 500 kDa solutions of dextran and water.

C.1 Evaporation

Since the solution reservoir had two open faces, water was evaporating from the solution under ambient conditions. A simple experiment was conducted to characterize this evaporation. All experiments were conducted in the lab between 22.5-24.0°C and at relative humidity less than 20%. A high precision balance scale was calibrated to the mass of the solution reservoir. Then, a 50 %wt solution of 500 kDa dextran in water was prepared using the same methodology as section 2.3. The solution reservoir was filled with this solution, and immediately placed back onto the scale. The mass reading from the scale was recorded in 30 second increments for 60 minutes. A concentration was calculated from these mass measurements using:

$$\%wt\ dextran = \left[\frac{mass_{dextran}}{mass_{total}}\right] \times 100\%. \tag{C.1}$$

As seen in Figure C.1, although the concentration continues to increase over time, within the first 10 minutes, the solution concentration changes less than 1 %wt. As such, the prepared solutions were always kept in a syringe to limit evaporation. When loaded into the reservoir, the solution was always completely replenished every 10 minutes in order to mitigate any effects of the evaporation.

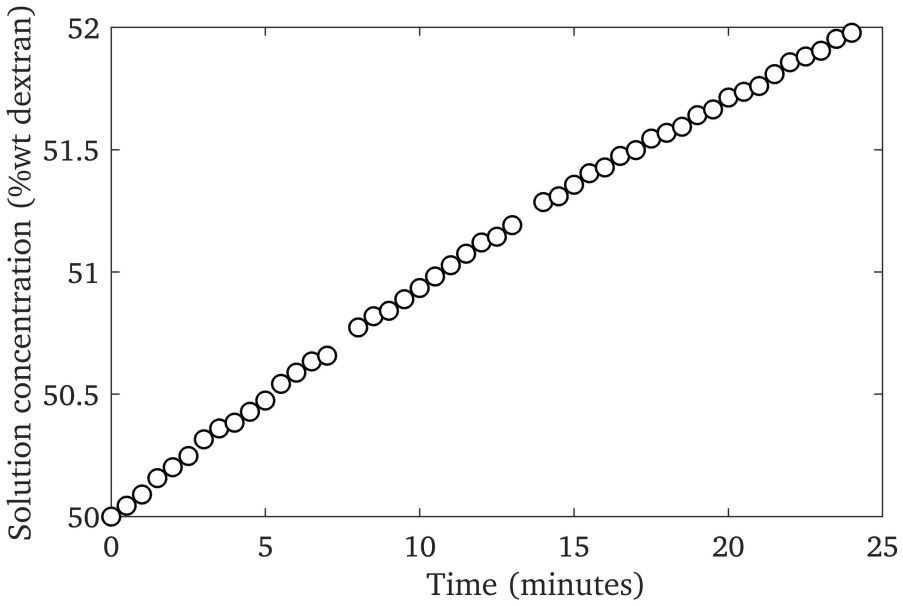

Figure C.1: *Solution concentration, as a function of time. In this experiment, 50 μL of 50 %wt 500 kDa dextran and water was placed in the reservoir. The reservoir was then loaded onto a scale and observed over time, and the loss of mass was recorded. Over the first 10 minutes, the change in solution concentration was less than 1 %wt dextran.*

C.2 Viscosity

The experiment in this section was conducted by Dr. John Frampton, who provided this data.

The bulk viscosity (η) of various solutions of 500 kDa dextran in water were measured using the falling ball method. 5 solutions were prepared at 35, 40, 45, 50, and 55 %wt dextran, in the same way as section 2.3. These solutions were then centrifuged at 3000 rcf for 15 minutes to remove any gas bubbles. The prepared solutions were transferred into polystyrene conical tubes.

Once in the tube, a stainless steel ball bearing (diameter = 0.3999 $\pm$ 0.002 cm and mass = 0.2611 $\pm$ 0.0001 g) was placed into the solution. With a digital timer accurate to 0.001 s and a ruler accurate to 0.5 cm, the position of the ball over time was recorded, and the velocity was calculated. The density of the solutions were measured using an Anton Parr DMA 35 handheld density meter, with an accuracy of 0.001 g/cm^3. With this data, η could be calculated using:

$$\eta = \frac{2\left(\Delta\rho\right) g r^2}{9v}, \tag{C.2}$$

where $\Delta\rho$ is the difference in density between the solution and the ball bearing, g is the acceleration due to gravity, r is the radius of the ball bearing, and v is the velocity of the ball bearing as it travels through the tube. This data is shown in Figure C.2. All solutions of 500 kDa dextran had concentrations within this range, so all values not directly measured were interpolated from the exponential fit.

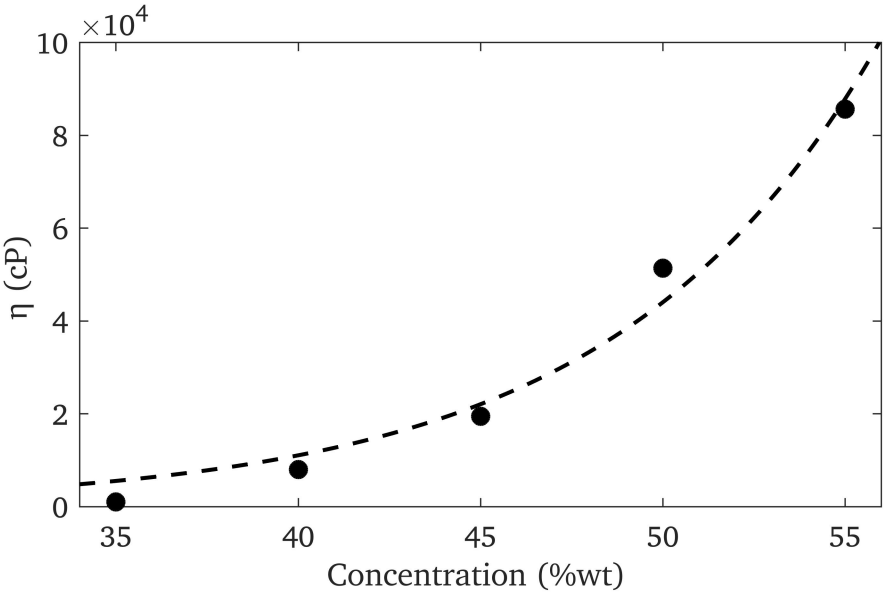

Figure C.2: *Viscosity as a function of concentration, courtesy of Dr. John Frampton. Viscosity data was measured for various concentrations of 500 kDa dextran in water, using the falling sphere method. Exponential fit is shown (dashed line, $r^2 = 0.98$).*

Appendix D

Copyright Permissions

Copyright Clearance Center Marketplace™

Royal Society of Chemistry - License Terms and Conditions

This is a License Agreement between Gurkaran Chowdhry ("You") and Royal Society of Chemistry ("Publisher") provided by Copyright Clearance Center ("CCC"). The license consists of your order details, the terms and conditions provided by Royal Society of Chemistry, and the CCC terms and conditions.

All payments must be made in full to CCC.

Order Date	21-Sep-2020	**Type of Use**	Republish in a thesis/dissertation
Order license ID	1064569-1		
ISSN	1744-6848	**Publisher**	ROYAL SOCIETY OF CHEMISTRY
		Portion	Image/photo/illustration

LICENSED CONTENT

Publication Title	Soft matter	**Country**	United Kingdom of Great Britain and Northern Ireland
Author/Editor	Royal Society of Chemistry (Great Britain)	**Rightsholder**	Royal Society of Chemistry
Date	06/01/2005	**Publication Type**	e-Journal
Language	English	**URL**	http://www.rsc.org/Publishing/Journals/sm/index.asp

REQUEST DETAILS

Portion Type	Image/photo/illustration	**Distribution**	Worldwide
Number of images / photos / illustrations	1	**Translation**	Original language of publication
Format (select all that apply)	Print, Electronic	**Copies for the disabled?**	No
		Minor editing privileges?	No
Who will republish the content?	Academic institution	**Incidental promotional use?**	No
Duration of Use	Life of current edition	**Currency**	USD
Lifetime Unit Quantity	Up to 499		
Rights Requested	Main product		

NEW WORK DETAILS

Title	Liquid bridge to stable fibre: polymer entanglement drives fibre formation from highly concentrated dextran solutions	**Institution name**	Dalhousie University
		Expected presentation date	2020-10-05
Instructor name	Laurent Kreplak		

A Combined Experimental and Numerical Modeling Study of the Deformation and Rupture of Axisymmetric Liquid Bridges under Coaxial Stretching

Author: Jinda Zhuang, Y. Sungtaek Ju
Publication: Langmuir
Publisher: American Chemical Society
Date: Sep 1, 2015

PERMISSION/LICENSE IS GRANTED FOR YOUR ORDER AT NO CHARGE

This type of permission/license, instead of the standard Terms & Conditions, is sent to you because no fee is being charged for your order. Please note the following:

- Permission is granted for your request in both print and electronic formats, and translations.
- If figures and/or tables were requested, they may be adapted or used in part.
- Please print this page for your records and send a copy of it to your publisher/graduate school.
- Appropriate credit for the requested material should be given as follows: "Reprinted (adapted) with permission from (COMPLETE REFERENCE CITATION). Copyright (YEAR) American Chemical Society." Insert appropriate information in place of the capitalized words.
- One-time permission is granted only for the use specified in your request. No additional uses are granted (such as derivative works or other editions). For any other uses, please submit a new request.

If credit is given to another source for the material you requested, permission must be obtained from that source.

BACK CLOSE WINDOW

Extensional Flow Behavior of Methylcellulose Solutions Containing Fibrils

Author: Svetlana Morozova, Peter W. Schmidt, Athena Metaxas, et al

Publication: ACS Macro Letters

Publisher: American Chemical Society

Date: Mar 1, 2018

PERMISSION/LICENSE IS GRANTED FOR YOUR ORDER AT NO CHARGE

This type of permission/license, instead of the standard Terms & Conditions, is sent to you because no fee is being charged for your order. Please note the following:

- Permission is granted for your request in both print and electronic formats, and translations.
- If figures and/or tables were requested, they may be adapted or used in part.
- Please print this page for your records and send a copy of it to your publisher/graduate school.
- Appropriate credit for the requested material should be given as follows: "Reprinted (adapted) with permission from (COMPLETE REFERENCE CITATION). Copyright (YEAR) American Chemical Society." Insert appropriate information in place of the capitalized words.
- One-time permission is granted only for the use specified in your request. No additional uses are granted (such as derivative works or other editions). For any other uses, please submit a new request.

If credit is given to another source for the material you requested, permission must be obtained from that source.

SPRINGER NATURE LICENSE
TERMS AND CONDITIONS

Sep 21, 2020

This Agreement between Dalhousie University -- Gurkaran Chowdhry ("You") and Springer Nature ("Springer Nature") consists of your license details and the terms and conditions provided by Springer Nature and Copyright Clearance Center.

License Number	4911900654260
License date	Sep 18, 2020
Licensed Content Publisher	Springer Nature
Licensed Content Publication	Rheologica Acta
Licensed Content Title	Structure and linear viscoelasticity of flexible polymer solutions: comparison of polyelectrolyte and neutral polymer solutions
Licensed Content Author	Ralph H. Colby
Licensed Content Date	Dec 29, 2009
Type of Use	Thesis/Dissertation
Requestor type	academic/university or research institute
Format	print and electronic
Portion	figures/tables/illustrations
Number of figures/tables/illustrations	1

ELSEVIER LICENSE
TERMS AND CONDITIONS

Sep 21, 2020

This Agreement between Dalhousie University -- Gurkaran Chowdhry ("You") and Elsevier ("Elsevier") consists of your license details and the terms and conditions provided by Elsevier and Copyright Clearance Center.

License Number	4912690981449
License date	Sep 19, 2020
Licensed Content Publisher	Elsevier
Licensed Content Publication	Advances in Colloid and Interface Science
Licensed Content Title	Dynamic wetting of dilute polymer solutions: The case of impacting droplets
Licensed Content Author	V. Bertola
Licensed Content Date	Jun 1, 2013
Licensed Content Volume	193
Licensed Content Issue	n/a
Licensed Content Pages	11
Start Page	1
End Page	11

Copyright Clearance Center | Marketplace™

Order Number: 1064067
Order Date: 18 Sep 2020

Payment Information

Gurkaran Chowdhry
chowdhry@dal.ca
Payment method: Invoice

Billing Address:
Mr. Gurkaran Chowdhry
3-6309 Quinpool Road
Halifax, NS B3L 1A4
Canada

+1 (416) 305-2801
chowdhry@dal.ca

Customer Location:
Mr. Gurkaran Chowdhry
3-6309 Quinpool Road
Halifax, NS B3L 1A4
Canada

Order Details

1. Journal of the Chemical Society. Faraday transactions II

Billing Status: Open

Order license ID	1064067-1
Order detail status	Completed
ISSN	0300-9238
Type of use	Republish in presentation/slides
Publisher	FARADAY DIVISION OF CHEMICAL SOCIETY,
Portion	Chart/graph/table/figure

0.00 USD
Republication Permission

LICENSED CONTENT

Publication Title	Journal of the Chemical Society. Faraday transactions II	**Country**	United Kingdom of Great Britain and Northern Ireland
Author/Editor	CHEMICAL SOCIETY (GREAT BRITAIN).,ROYAL SOCIETY OF CHEMISTRY (GREAT BRITAIN).	**Rightsholder**	Royal Society of Chemistry
		Publication Type	Journal
Date	01/01/1972		
Language	English		

REQUEST DETAILS

Portion Type	Chart/graph/table/figure	**Distribution**	Worldwide
		Translation	Original language of publication

ELSEVIER LICENSE
TERMS AND CONDITIONS

Sep 21, 2020

This Agreement between Dalhousie University -- Gurkaran Chowdhry ("You") and Elsevier ("Elsevier") consists of your license details and the terms and conditions provided by Elsevier and Copyright Clearance Center.

License Number	4912071233900
License date	Sep 18, 2020
Licensed Content Publisher	Elsevier
Licensed Content Publication	Journal of Electrostatics
Licensed Content Title	Fiber diameter in electrospinning process
Licensed Content Author	Bogdan Cramariuc,Radu Cramariuc,Roxana Scarlet,Liliana Rozemarie Manea,Iuliana G. Lupu,Oana Cramariuc
Licensed Content Date	Jun 1, 2013
Licensed Content Volume	71
Licensed Content Issue	3
Licensed Content Pages	10
Start Page	189
End Page	198